AD_____

Award Number: W81XWH-13-1-0127

TITLE: Magnetic Resonance-Based Electrical Property Tomography (MR- EPT) for Prostate Cancer Grade Imaging

PRINCIPAL INVESTIGATOR: Ryan Halter

CONTRACTING ORGANIZATION: Trustees Of Dartmouth College

Hanover, NH 03755-4099

REPORT DATE: July 2014

TYPE OF REPORT: Annual

PREPARED FOR: U.S. Army Medical Research and Materiel Command
Fort Detrick, Maryland 21702-5012

# REPORT DOCUMENTATION PAGE

*Form Approved*
*OMB No. 0704-0188*



| 1. REPORT DATE | 2. REPORT TYPE | 3. DATES COVERED |
|---|---|---|
| July 2014 | Annual | July 1, 2013 – June 30, 2014 |

**4. TITLE AND SUBTITLE**
Magnetic Resonance-Based Electrical Property Tomography (MR- EPT) for Prostate Cancer Grade Imaging

**5a. CONTRACT NUMBER**

**5b. GRANT NUMBER**
W81XWH-13-1-0127

**5c. PROGRAM ELEMENT NUMBER**

**6. AUTHOR(S)**
Ryan Halter
Betty Diamond

E-Mail: ryan.halter@dartmouth.edu

**5d. PROJECT NUMBER**

**5e. TASK NUMBER**

**5f. WORK UNIT NUMBER**

**7. PERFORMING ORGANIZATION NAME(S) AND ADDRESS(ES)**
Trustees of Dartmouth College

Hanover, NH 03755-4099

**8. PERFORMING ORGANIZATION REPORT NUMBER**

**9. SPONSORING / MONITORING AGENCY NAME(S) AND ADDRESS(ES)**
U.S. Army Medical Research and Materiel Command
Fort Detrick, Maryland 21702-5012

**10. SPONSOR/MONITOR'S ACRONYM(S)**

**11. SPONSOR/MONITOR'S REPORT NUMBER(S)**

**12. DISTRIBUTION / AVAILABILITY STATEMENT**
Approved for Public Release; Distribution Unlimited

**13. SUPPLEMENTARY NOTES**

**14. ABSTRACT**
Determining whether a man recently diagnosed with prostate cancer has aggressive disease requiring immediately radical therapy or indolent disease requiring a more passive watchful waiting or active surveillance approach is a current clinical challenge. This technology development study is focused on developing Magnetic Resonance – Electrical Property Tomography (MR-EPT) specifically for prostate imaging. MR-EPT is an imaging modality that may enable clinicians to image the electrical properties of prostate at near MR resolution. These electrical properties are hypothesized to provide sufficient contrast for distinguishing between aggressive and indolent prostate cancer. Much of the first year of this program has focused on MR sequence optimization, MR-EPT image reconstruction algorithm development and optimization, experimental imaging of both simplistic and anatomically accurate phantoms, and initial ex vivo prostate imaging. During this year we have optimized our MR-EPT sequences, demonstrated the imaging capabilities of MR-EPT through phantom studies, and have produced the first conductivity images of ex vivo prostate using MR-EPT techniques. The second year of the program will primarily focus on ex vivo and in vivo data acquisition, statistical analysis of our data, and preparation of publications and proposals for follow-on more clinically focused studies.

**15. SUBJECT TERMS** nothing listed

| 16. SECURITY CLASSIFICATION OF: | | | 17. LIMITATION OF ABSTRACT | 18. NUMBER OF PAGES | 19a. NAME OF RESPONSIBLE PERSON |
|---|---|---|---|---|---|
| a. REPORT | b. ABSTRACT | c. THIS PAGE | | | USAMRMC |
| U | U | U | UU | 41 | 19b. TELEPHONE NUMBER *(include area code)* |

**Table of Contents**

## INTRODUCTION

This program builds off of our extensive experience in using electrical properties of prostate to distinguish malignant from benign tissues [1-5] and specifically stems from exciting new data published in The Prostate [6] in which we demonstrated significant electrical property differences between high- and low-grade prostate cancer. These electrical properties are influenced by a tissue's intra- and extra-cellular composition, morphology, and cellular constituency, and we have hypothesize that it is possible to use these properties to discriminate between normal, low-grade, and high-grade malignant formations in a clinical setting. While measuring these properties by direct contact with the tissues is possible in invasive experiments, it is desirable to develop methods to do so in a non-invasive fashion. To date our group, and other groups around the world, have investigated Electrical Impedance Tomography and Microwave Imaging, two techniques which are limited in resolution by the underlying physics. The primary objective of this current program is to develop a high-resolution MR-based approach to imaging the electrical properties of prostate with the intent of producing a system potentially able to image cancer grade. This is possible by leveraging ultra-novel developments in MRI, and our extensive experience in developing technologies to gauge and assess the utility of electrical properties for prostate cancer detection [1-6] and assessment and in developing computer algorithms to transform electromagnetic data into electrical property images of the prostate [7-14]. Specifically, we are attempting to use the maps of MRI RF field data acquired with safe and fast sequences to create high-resolution electrical property images of the prostate. We are developing this novel technology, evaluating it in an *ex vivo* setting, and finally assessing the feasibility of employing this imaging modality in a routine clinical cohort of patients with the intent of having a significant and immediate impact on clinical practice. By developing this high-resolution electrical property imaging modality we expect to produce highly sensitive and specific images of cancer grade within the prostate and ultimately better guide clinicians in distinguishing aggressive from indolent disease.

Much of the first year of this program has focused on MR sequence optimization, MR-EPT image reconstruction algorithm development and optimization, experimental imaging of both simplistic and anatomically accurate phantoms, and initial ex vivo prostate imaging. The second year of the program will primarily focus on ex vivo and in vivo data acquisition, statistical analysis of our data, and preparation of publications and proposals focused more heavily on clinical data acquisition and evaluation.

## BODY

The following research summary is presented in terms of the approved Statement of Work, with each task being discussed separately. When appropriate, detailed discussion is referenced to manuscripts published, submitted, or in preparation which are provided in the Appendix. Note that future task and objectives to be completed are marked as **TBC**.

### *SPECIFIC AIM 1: TO DEVELOP MR-EPT FOR PROSTATE IMAGING*

#### Major Task 1: Develop computation toolbox for MR-EPT

a) Build Matlab-based toolbox for computing electrical property images

*We have fully implemented our proposed method as a MATLAB toolbox for MR-EPT image reconstruction. In addition, we have implemented several other approaches that we have been using to demonstrate how our implementation is superior; specifically we have:*

- *Implemented an Average Laplacian approach which takes the Laplacian (which is proportional to the conductivity) and smooths it with a Gaussian spatial filter to reduce noise.*
- *Implemented a Surface Integral Gradient approach which is an algorithm equivalent to one developed by Ulrich Katscher [15]. Specifically, the Gauss theorem is used to transform a volume integral of the Laplacian into a surface integral of the gradient of the phase and therefore reduce differentiation from a second order to first order problem; this effectively reduces how noise influences the image is generated.*
- *Developed and implemented our Inverse Problem with Quadratic Regularization.*
- *Developed and implemented an Inverse Problem Approach with Total Variation (TV) Regularization; this improves image resolution at high contrast boundaries and demonstrates that advanced regularization schemes can be implemented with an inverse problem approach to solving the MR-EPT problem. One exciting outcome of this development is that we can use spatial information from other MR variants (i.e. T2-weighted) to help drive our estimation of the electrical properties distribution.*

- *Conducted laboratory experiments to test on real data the newly developed approach, showing improved reconstructed images against implementations of the algorithms developed in the literature.*

*The underlying development of these algorithms are described in detail in Appendix 1.*

***Simulation Results:***

*We have evaluated three of the reconstruction approaches in terms of their ability to accurately reproduce a step change in conductivity in the presence of noisy data. Specifically, we have developed a test case represented by a step change in conductivity – this would for instance represent a step change between the prostatic boundary and peri-prostatic adipose tissue (where the conductivity contrast may be as high as 10:1 or 100:1). Figure 1 shows the results of this evaluation. Our inverse approach, with both Quadratic and TV regularization, provides a better estimate of the conductivity transition than the Average Laplacian approach. In addition, TV regularization is able to produce a steeper transition than the other approaches (Figure 2). The ability to reproduce a steeper transition will translate into a higher imaging resolution at boundaries of large conductivity transitions. The final item to note, is that the inverse approaches are able to tolerate higher levels of data noise than the Average Laplacian approach. The 10% noise figure represents an extremely high level of noise that we do not expect to have during clinical image acquisition and instead represents a worst-case scenario.* For more details on the algorithm developed please see Appendices.

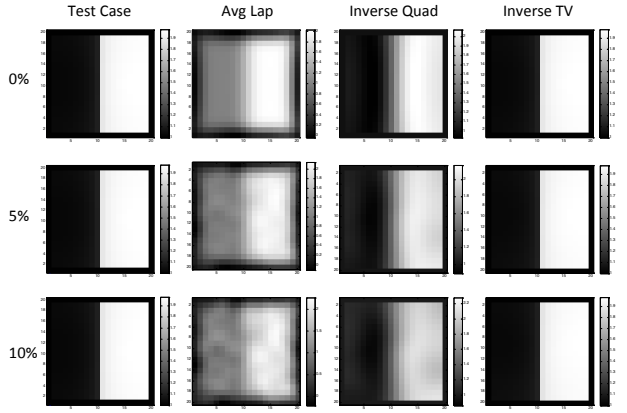


**Figure 1:** Simulation evaluation of step change in conductivity. Three reconstruction algorithms are compared in the presence of three different levels of Gaussian noise added to the MR-recorded phase data (0%, 5%, and 10%). The algorithms compared include the Average Laplacian (Avg Lap), the Inverse Problem with Quadratic Regularization (Inverse Quad), and the Inverse Problem with Total Variation Regularization (Inverse TV) approaches.

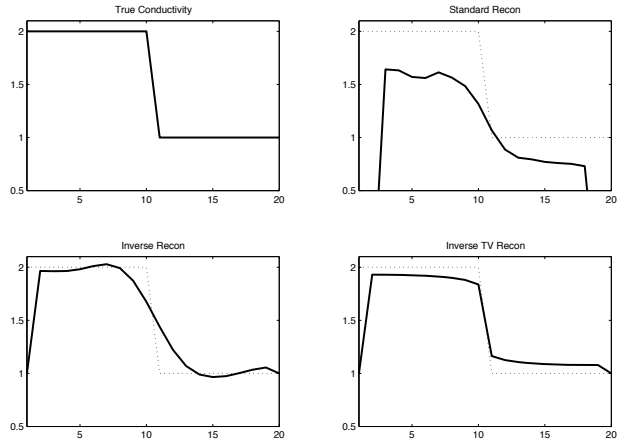


**Figure 2:** Cross-section of reconstructed conductivity (based on simulations). Note that the Inverse Recon and Inverse TV Recon estimate the True Conductivity profile better that the Standard Recon approach based on a finite difference approach only.

b) Build Matlab-based toolbox for specific MR-based field of views

*We have developed Matlab-based functions to read in arbitrary MRI DICOM and .PAR/.REC (Phillips format) images and display them for evaluation. Additional developments have included the ability to create multi-slice images of the MR data for use in comparing the different MR variants we are exploring (e.g. Figure 3).*

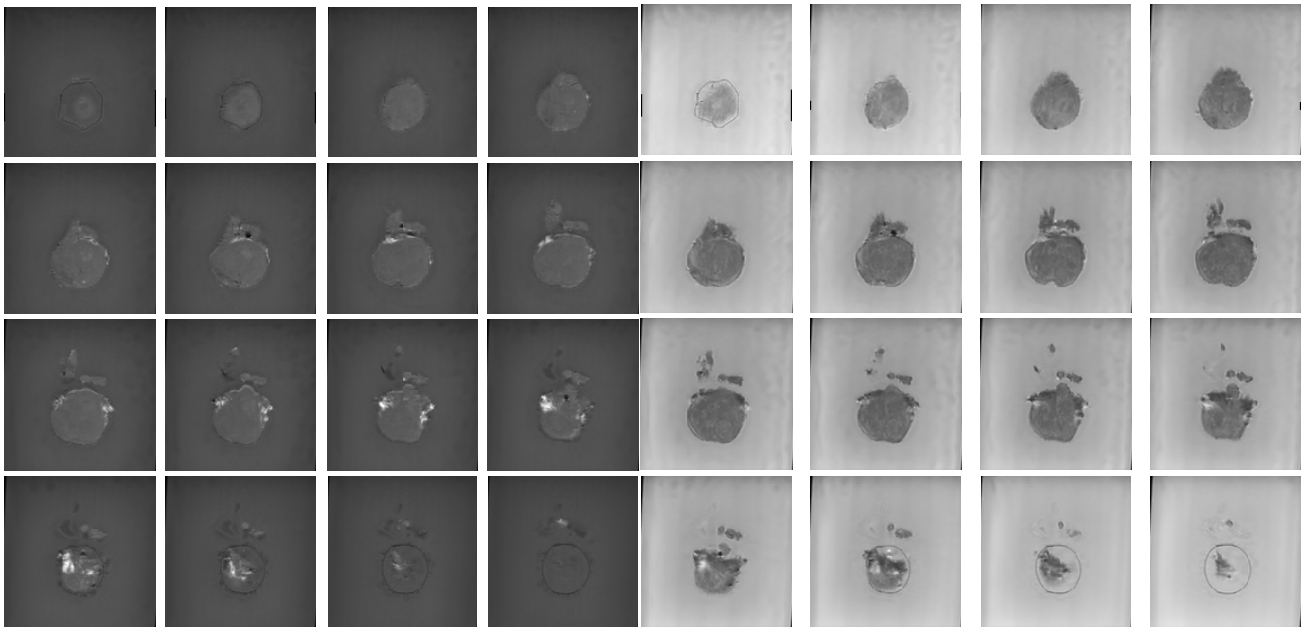

**Figure 3.** Exported panels for displaying a sequence of MR images. This example shows T1 (left) and T2 (right) image stacks of an ex vivo prostate recorded as part of our ex vivo study cohort. Our Matlab display scripts allow a user to input an MR image stack for display, including our MR-EPT images.

***Task 1 Milestones:***

1. Functional toolbox for producing MR-EPT images **– Completed**

**Major Task 2: Optimize MR-EPT and multi-parametric MR imaging through phantom imaging**

a) Optimize MR-sequence for MR-EPT

*We have determined an optimal MR sequence to use for acquiring MR-EPT data from our ex vivo and in vivo cohorts. The main concern at this point remains the length of the acquisition required to gather all the necessary imaging data (T2 anatomical, MR-EPT, DWI, and spectroscopy) with sufficient signal-to-noise ratios. We have found that the MR-EPT images are very dependent on the B-field magnitude images; the highest quality MR-EPT images are computed when multiple B-field magnitude images are averaged together. We have worked to optimize the balance between voxel size (resolution) and the number of repetitions (acquisition time) required to obtain sufficient signal-to-noise ratio and resolution. We have two pulse sequences that we have found to be optimal for reconstructing MR-EPT conductivity images:*

I. *Spin Echo (SE) – **pros:** less prone to artifacts, less time consuming, **cons:** less sharp contrast for conductivity.*
II. *3D Turbo Spin Echo (TSE) - **pros:** gives sharper conductivity contrast, **cons:** long acquisition time, prone to imaging artifacts*

*The MREPT approach for reconstructing conductivity is based on processing phase data collected with specific pulse sequences as described here. The optimal Spin Echo (SE) multi-slice sequence consists of a sequence with TR=800, TE=20, and has a flip angle of $90^o$. The second optimal option we have explored is the Turbo Spin Echo (TSE) 3D sequence with a Turbo factor of 3 and a flip angle of $90^o$ (TR=239,TE=17). We currently acquire 8 or 16 signal averages (NSA=8 or 16) in both cases to achieve a sufficiently high SNR. However, if the scan duration is too long (>1h), especially in the TSE sequence case, we reduce the signal averages (i.e. NSA=8). Data is acquired with a flex coil (one transmit, one receive channel); no endorectal coil is being used as our Radiologist Co-Investigator informed us this is not currently in use at DHMC and does not provide significantly better SNR. In all scans, we place our phantoms and ex vivo prostates in an orientation similar to how a patient is positioned during a routine prostate scan (for the ease of comparison with subsequent clinical data): head-first supine, with 'transverse' slices (from seminal vesicles to the apex of the prostate), fold-over direction AP, fat shift direction L. Currently, our preferred voxel size is 2x2x3mm (a 3mm imaging slice thickness is clinically used). The corresponding reconstructed voxel size is 2x2x3mm. The field of view (FOV) and number of slices influence the scan duration as well. As an example, acquiring a scanning a typically sized phantom (or imaging volume) with the above*

*mentioned parameters, having a stack of 25 slices, and a FOV of 130x130x75mm requires a total scan duration of 1:00.16 for the TSE sequence and 27:48.8 for the SE sequence. Although the TSE tends to result in sharper contrasts in the reconstructed conductivity maps, its duration makes it difficult to use for the future in vivo study; we have therefore opted to use the SE sequence for our initial set of ex vivo experiments.*

b) Perform initial tank-based phantom imaging studies

*A number of tank-based phantom studies were conducted during the early stages of this program to demonstrate that our MR-EPT algorithms are able to accurately estimate the internal conductivity of a volume. Two types of initial phantom studies conducted are described below (many additional phantom studies were conducted as part of this research, but are not included here). Additional details regarding phantom experiments and analysis are provided in Appendices 2-5.*

*<u>Saline Tank:</u> We have conduted several saline tank experiments in the process of developing and optimizing our pulse sequences and reconstruction algorithms. We assessed how accurate our algorithms are at estimating the electrical properties of uniform saline phantoms with a known electrical conductivity (measured using a conductivity meter, Oakton CON 2700, Vernon Hills, Il). The process is exemplified in Figure 4. Specifically, the conductivity is determined by fitting parabolas to the i, j, and k-axes of the acquired phase image. By manipulating the coefficients describing these parabolas we estimate the coductivty. Our image reconstruction algorithms perform a similar fitting on a pixel basis when used to form volumetric images. In these saline tank experiments, the errors between the electrical conductivity computed with our in-house developed Matlab-based MR-EPT code described above and the measured values are < 10%.*

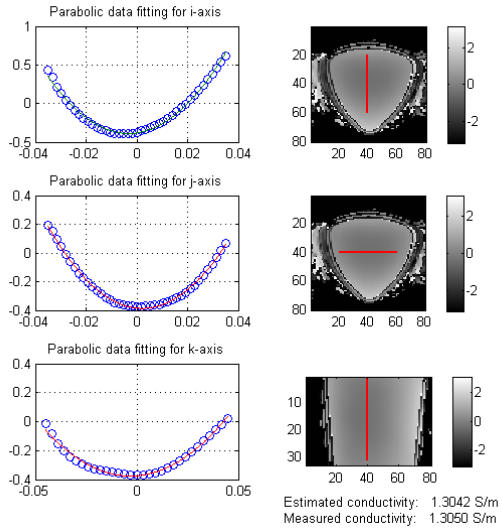


**Figure 4.** Phase images of a saline phantom (right column); each image represents each of the 3 axis i, j, k. Parabolic phase data (left column) extracted from each of the phase images (red line); these parabolas are used for conductivity estimation as described above. The solution had a measured conductivity 1.304 S/m. The estimated conductivity was 1.1305 S/m representing an error of <1% with respect to the know solution conductivity.

*<u>Striped Phantom:</u> Our pulse sequences and algorithms were further vetted using a more heterogeneous phantom. Specifically, a striped gelatin phantom was generated by cutting a cube of gelatin into multiple slices of progressively increasing thickness' of 5 mm, 10 mm, 15 mm, and 20 mm (Figure 5). NaCl was added to the gelatin mixture prior to setting to provide a conductivity of approximately 1.8 S/m. The container holding the slices was filled with a saline solution having a conductivity of 4.1 S/m; this produced a conductivity contrast of approximately 2 to 1 with respect to the gelatin (this contrast is similar to that expected within the prostate, based on our previous findings in ex vivo prostate sample). Additionally $CuSO_4$ was added to the gelatin (this boosts the "normal" MRI signal but does not affect MR-EPT) and no*

*$CuSO_4$ was added to the saline solution. We were able to successfully reconstruct the conductivity distribution of the striped geometry using our developed MR-EPT algorithms (Figure 5). As expected, the TV approach provided the best estimation of the step change. However, within the prostate we don't expect step changes in conductivity to be the norm and will likely find that the Quadratic Regularization is more optimal for clinical use. Both of these will be used during our exploration of our ex vivo and in vivo data.*

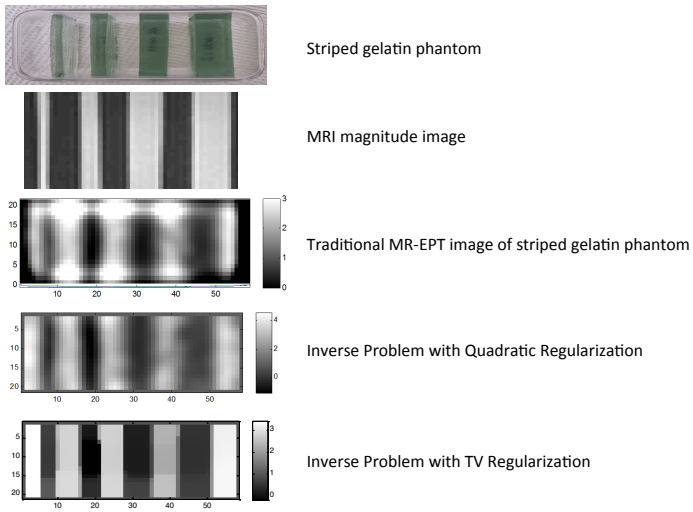


**Figure 5:** Reconstruction of our striped gelatin phantom. Note that the TV regularized method produces a much more uniform conductivity distribution within the different regions and depicts a more accurate step transitions between the saline background and the gelatin blocks.

c) Perform anatomically accurate phantom imaging studies

*A number of complex phantoms were generated to investigate the capabilities and limitations of our MR-EPT developments. These phantom studies consisted of a contrast-resolution phantom (hybrid of gelatin and saline), several prostate-shaped gelatin phantoms harboring different inclusions, ex vivo animal tissue models, and in vivo human calf imaging. Some of these phantoms were used during MR sequence optimization, while others were more recently used to demonstrate effectiveness of MR-EPT to image conductivity in biological tissues. Below we provide details regarding each of these phantoms.*

*<u>Contrast-Resolution Phantom:</u>*

*We developed a Contrast-Resolution (CR) Phantom to evaluate MR-EPT on a more heterogeneous volume (Figure 6). Specifically, we generated a mold that enables us to produce a gelatin substrate with multiple holes with varying diameters. The phantom includes three rows of similarly sized holes (5 mm, 10 mm, and 15 mm). A second phantom was also constructed to explore smaller diameter holes (1 mm, 2 mm, 3 mm, 4 mm); however, we have not yet evaluated this phantom and plan to do so over the next reporting period. The holes can be filled with solutions having different electrical/MR properties.*

*In an example experiment (Figure 6), the left-most, center, and right-most holes were filled with three different saline solutions having conductivities of 3.85 S/m, 5.12 S/m, and 7.56 S/m, respectively. The copper sulfate concentration in each of the saline solutions was the same. The gelatin had a conductivity of ~2 S/m. Based on the experimental setup we expected to observe the following: 1) the MR-magnitude should be the same for all holes because the copper sulfate concentrations were the same, 2) the holes should have a higher conductivity than the background, and 3) the left-most holes should have the lowest conductivity and the right-most holes should have the highest conductivity. The following observations were made regarding this evaluation:*

1) *MR magnitude images (Figure 6.c) show that the MR magnitude is constant for the different solutions as expected and that it is greater than the background where no copper sulfate was used.*

2) *A single parabola accurately fit the phase profile (used for conductivity estimation as described above) within the homogenous gelatin background of the CR phantom (Figure 6.d)*
3) *Multiple parabolas can be concatenated to fit the phase profile through the rows of holes in the phantom (Figure 6.e). The multiple parabolas are more easily observed in the row with the larger holes (15 mm).*
4) *Our inverse approach to solving producing and MR-EPT image is able to identify the conductivity contrast at all three hole sizes (Figure 7.a). The smallest diameter holes (5 mm) are easily visualized which suggest that we will be able to identify smaller conductivity contrasts more in line with what is expected in the prostate. In addition, the conductivity within the reconstructed holes increases from left to right as expected. This represents an exciting development – Namely, in regions where there is no MR-contrast, but conductivity contrast exists, MR-EPT is able to identify the different levels of conductivity, while MR-magnitude imaging shows no variation. (Here the holes have the same MR-magnitude, while the holes in the conductivity images vary as the solution conductivity varies). The potential clinical implications for this in regarding to prostate imaging are that tissues may have very small MR-contrast, but a large conductivity contrast. In these cases, MR-magnitude imaging would not be a viable technique for identifying the different tissues types, while MR-EPT would be able to identify the different tissues.*
5) *TV regularization (Figure 7.b) provides more uniform conductivity distribution within the solutions and background and more accurate transitions between background and solution regions.*
6) *There are artifacts surrounding the holes within the MR-EPT images. These artifacts increase for larger conductivity solutions. These arise from assumptions used to simplify the conductivity estimation algorithms used to model the underlying physics. Specifically, the conductivity is assumed continuous over the volume in which the conductivity is being estimated. At these step changes in conductivity, the conductivity distribution is not continuous; as a result these "shadow" artifacts appear at these boundaries. One method to address these artifacts may be to incorporate a priori information (e.g. T1w or T2w) to help "guide" the reconstruction. This is an interesting line of research we hope to follow in the upcoming year. Another approach to overcome these artifacts would be to solve a more complex physical problem that does not required the conductivity continuity assumption. This area of research is likely beyond the scope of the current program, but would be interesting to explore in follow-on research efforts.*

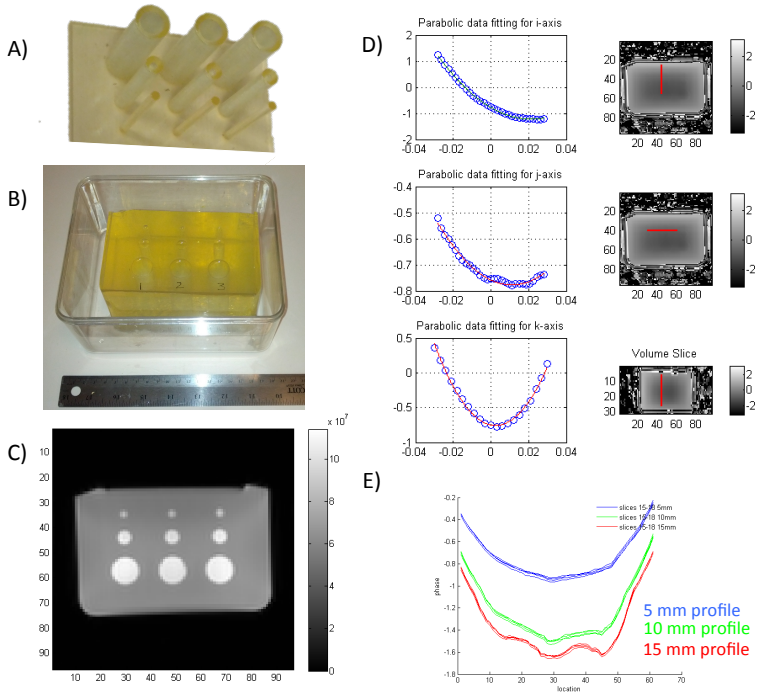


**Figure 6:** Contrast-Resolution (CR) Phantom. A) Rapid prototype mold for use in generating gelatin CR phantoms. B) Gelatin phantom filled with three different saline solutions; hole 1 = 3.85 S/m, hole 2 = 5.12 S/m. hole 3 = 7.56 S/m. Each solution had the same quantity of copper sulfate. C) T1w MR magnitude image. Note that the background MR signatures are equivalent for each of the holes. D) Parabolic fitting within the gelatin background; the parabolic fit is fairly homogenous in the homogenous gelatin background as expected. E) Parabolic fitting through each row of holes. The blue, green, and red profiles correspond to the 5 mm row, 10 mm row, and 15 mm row, respectively. The multiple traces associated with each row are produced at different z-levels demonstrating uniformity in the phase image along the depth of the phantom.

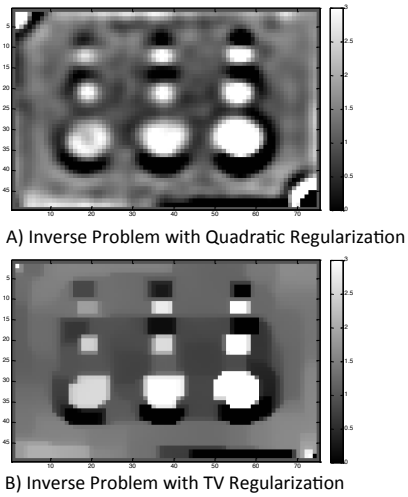


**Figure 7:** MR-EPT images of the CR phantom computed using our developed inverse problem based approach. A) Quadratic regularization, B) TV regularization.

*Additional images have been acquired with these contrast resolution phantoms to further compare the different MR-EPT reconstruction algorithms. In one example (Figure 8), the wells were filled with similar conductivities (as above), namely: 1) 8 S/m (top row), 2) 5 S/m (middle row), 3) 3 S/m (bottom row). Figure 8 shows the reconstructed conductivity maps with the different MR-EPT reconstruction approaches we have developed.*

*Observations from this experiment include:*

1. *The MR magnitude image shows contrast between the saline and gelatin, but no differences were noted between the different saline solutions.*
2. *MR-EPT conductivity images show the expected relationships between the different saline solutions – the top (8 S/m) well has the highest conductivity followed by the middle (5 S/m) and bottom (3 S/m) wells.*
3. *The reconstructed conductivity values approach the true conductivity values measured with a conductivity meter outside of the MRI (see scale bar for comparison).*

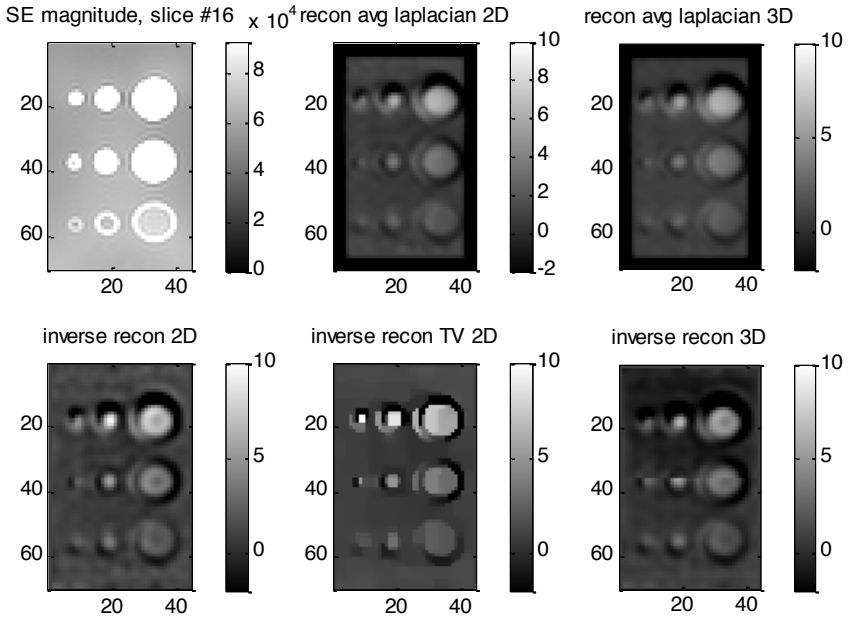


**Figure 8.** SE magnitude image and reconstructions: 2D average Laplacian, 3D average laplacian, 2D inverse reconstruction, 2D inverse reconstruction with Total Variation, 3D inverse reconstruction

*Anatomically Accurate Gelatin Phantoms:*

*We have constructed a silicone prostate mold based on segmented CT images of a man's prostate. Within the mold we are able to produce gelatin prostates that accurately model true anatomy. The gelatin prostates can be made to be heterogeneous by using gelatins formed from different conductivity saline solution or by embedding high or low contrast inclusions within the gelatin while it is setting. A number of experiments have been conducted on these anatomically accurate prostate models for use in evaluating and optimizing MR-EPT for prostate imaging.*

a) *Two regions of different conductivities*

*This phantom consists of a gelatin prostate comprising two regions of different conductivities: 1.6 S/m (pink) and 3.4 S/m (blue) (see Figure 9). The phantoms were constructed by adding different quantities of NaCl to the gelatin mixtures. Once formed, the phantom prostate was submerged in deionized water and supported and kept in place by a paper ring stand; the stand provides virtually no MR signal and has minimal contact with the phantom.*

*Phase images were acquired with both SE and TSE sequences to compare the two. The five different reconstruction algorithms we have been exploring were used to compute conductivity maps. Figure 9 displays the magnitude images along with the reconstructed conductivity maps for both SE and TSE. It is clear that images based on SE acquisition are superior to TSE. In this experiment there was no difference in MR contrast between the two halves of the prostate, but there was conductivity contrast. As expected, the MR magnitude images show primarily a homogenous prostate, while the conductivity images (based on SE data) show a region of high conductivity on the left (corresponding to the blue gelatin = 3.4 S/m) and a region of low conductivity on the right (corresponding to the pink gelatin = 1.6 S/m). Visually, it appears that the 'recon avg laplacian 3D' and 'inverse recon 3D' are the best algorithms to use in this case. This represents an exciting finding demonstrating that MR-EPT is able to image contrasting conductivities media even when there is no MR contrast.*

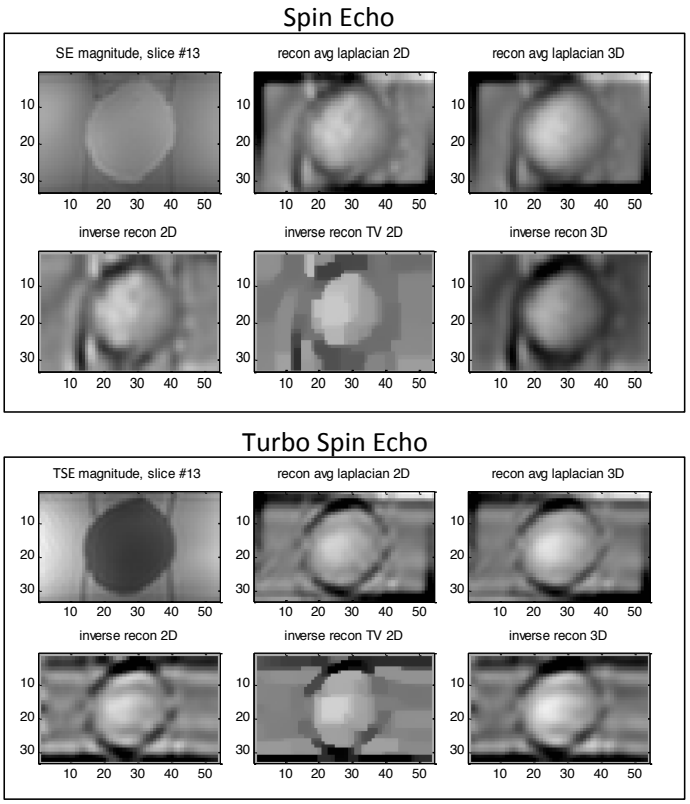


**Figure 9.** Gelatin phantom prostate-shaped with two regions of different conductivity ready to scan (left). Conductivity for blue side and pink side are # S/m and # S/m, respectively. Geometry and conductivity reconstructions (top right - SE data, bottom right – TSE data). Note that conductivity images based on SE acquisition provide a more accurate estimate of the conductivity distribution than when TSE sequences are used.

b) *Single inclusion*

*A single 5 mm diameter inclusion (play dough to provide significant conductivity contrast, lower than gelatine) was embedded in a gelatin prostate with a conductivity of approximately 2 S/m. Figure 10 shows TSE magnitude and reconstruction results. Each pixel is 3 mm x 3 mm (x 3mm for the voxel). Despite the lower resolution (than the 2x2x3) discussed above), this voxel size was explored here to explore how we might reduce scan time (it was still ~45 minutes for 16 time repetitions which will likely not be reasonable for in-vivo exams). The reconstructions appear geometrically accurate (both the gelatin prostate and the inclusion are identifiable within the conductivity images) however the spatial distribution of conductivity is somewhat reduced by the larger pixel size.*

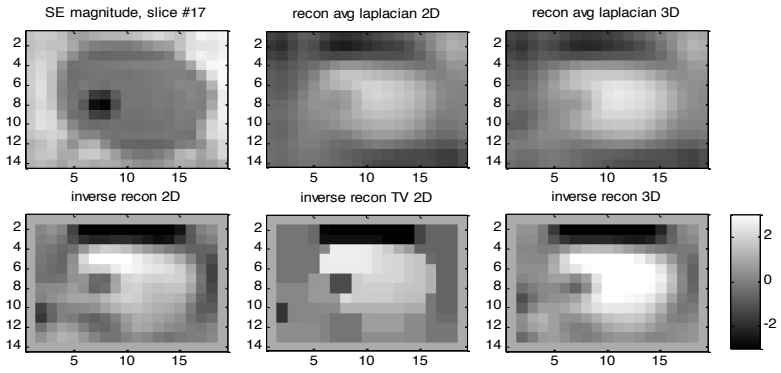


**Figure 10.** Prostate-like gelatin phantom with one inclusion (5mm, play dough), magnitude image (TSE) and reconstructions.

c) *Multiple Inclusions*

*Two 5 mm diameter inclusions (play dough to provide significant conductivity contrast, lower than gelatine) were embedded in a gelatin prostate with a conductivity of approximately 2 S/m. Figure 11 shows SE sequence magnitude and reconstruction results. Each pixel is 2 mm x 2 mm (x 3mm for the voxel). The reconstructions appear geometrically accurate (both the gelatin prostate and the inclusions are identifiable within the conductivity images). Both inclusions are identifiable in the conductivity images. We have observed some variation in the k-axis that we are still trying to identify the cause. This may be an artifact of spatial encoding used in this direction. Despite this, the inclusions are observable in the conductivity images. To mitigate this axial variance we may normalize all images and determine thresholds based on the normalized images. This will be explored as part of our on-going phantom work and as we begin to analyze our clinical data.*

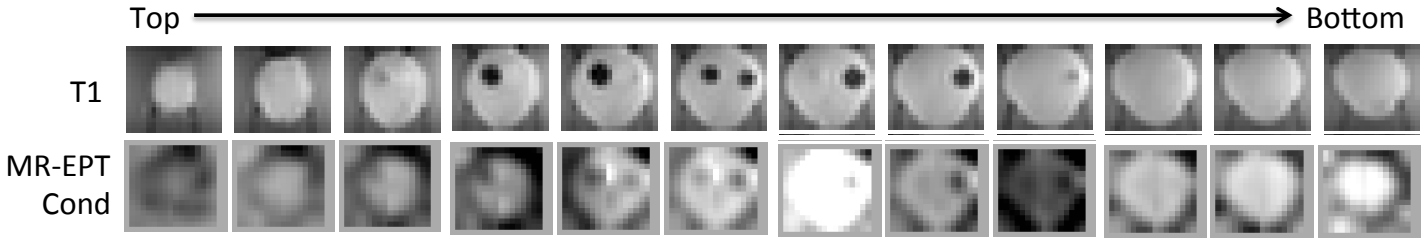


**Figure 11.** Multi-inclusion gelatin phantom. Top row shows T1 MR images along the axis of phantom; two playdough inclusions at different planes show up as low intensity regions. Bottom row shows MR-EPT conductivity images. The playdough inclusions show up as low conductivity inclusions. Note that there is axial variability within the conductivity images (potential due to spatial encoding artifacts) that is still being explored.

*Ex Vivo Animal Tissue Phantoms*

a) *Bovine Muscle/Adipose:*

*Data was acquired from a cuboidal specimen of ex vivo bovine to evaluate how well MR-EPT is able to differentiate between various components in a biological setting. The tissue specimen specifically was comprised of muscle fibers and adipose tissue. A 3x3x3 voxel size was again explore here. The specimen margins were well localized within the image and areas of adipose tissue around the periphery of the tissue were identified (Figure 12). Internal adipose tissue was less readily identifiable. Further experiments are needed in order to optimize the acquisition voxel size for maximum SNR. The general lack of conductivity contrast of the phantom and a rather large voxel size (3x3x3 mm) lead to a conductivity reconstruction that lacks some of the geometrical accuracy.*

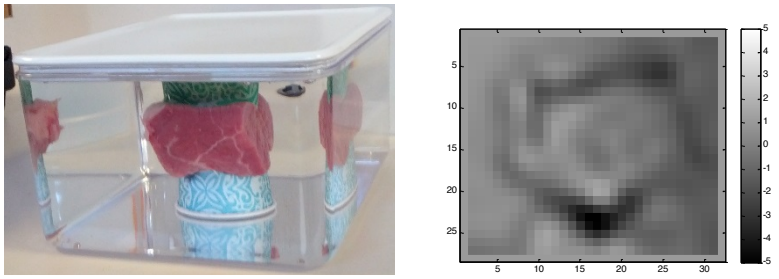

**Figure 12.** Meat phantom and 3D inverse reconstruction of the conductivity

b) *Bovine Kidney:*

*A fresh ex-vivo bovine kidney has been imaged in the same configuration in which we conduct our ex-vivo prostate experiments – immersed in deionized water. The T2w image, RF magnitude image and conductivity map are presented in* Figure *. The conductivity images show the anatomy of the kidney including both the parenchymal regions (higher conductivity) and the highly fibrous collecting system (lower conductivity).*

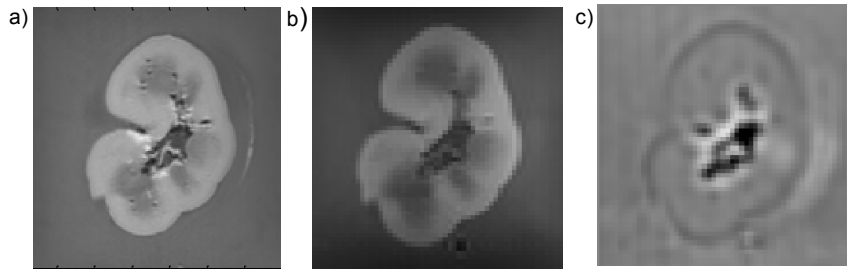


**Figure 13.** Bovine kidney magnitude images and conductivity reconstruction map: a) anatomical T2 image (resolution 1x1x3mm) – central dark region contains the fibrous collecting system; b) MR-EPT magnitude (resolution 2x2x3mm); c) conductivity map – to be noticed the reconstruction artifacts - the light ring around the central region and darker ring around the boundary.

*Observations from this experiment include:*

1. *The T2 magnitude image shows more geometrical detail due to its increased resolution. The resolution loss in the MR-EPT magnitude image is balanced by an increased SNR.*
2. *The MR-EPT conductivity map highlights the existence of the reconstruction artifacts due to abrupt changes in conductivity in the geometry: on one hand the slight jump between the low electrical conductivity of tissue to the almost zero conductivity of deionized water, and on the other hand the higher jump in the central region due to the change in conductivity from kidney parenchyma to the fibrous collecting system (also containing some adipose tissue) that combines with a fat imaging artifact (common in MR sequences) to give rise to the 'high' conductivity ring around the central area.*
3. *The reconstructed conductivity values of the kidney parenchyma (0.1-0.3 S/m) are in the range expected of kidney tissues.*
4. *We do not expect to encounter extensive intraprostatic artifacts within our clinical ex vivo or in vivo prostate scans due to the presence of fat; there is typically very little adipose tissue within the prostate.*

*In vivo (human) calf muscle*

*We have an active IRB-approved protocol at Dartmouth that enables researchers to evaluate new MR pulse sequences on healthy volunteers to help speed the R&D effort required to optimize a sequence prior to using it in a pre-clinical trial. We leveraged this resource to record MR-EPT data from a healthy volunteer and reconstructed the conductivity maps in order to evaluate our approach in an in vivo system. Specifically, in order to monitor the quality of conductivity reconstructions for a rather large and relatively homogeneous tissue region we conducted acquired MR image data of the muscles in a healthy human calf. The reconstruction of the conductivity along with the anatomy captured by a T2 image are shown in* Figure . *Interestingly, the reconstructed conductivity images are able to accurately distinguish between the different muscle bundles.*

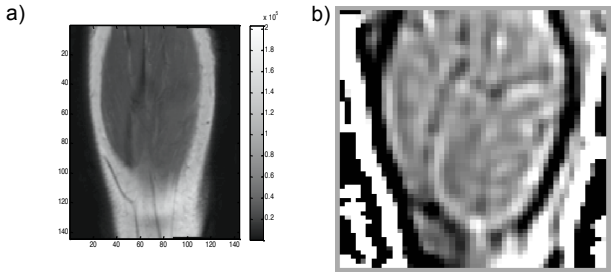


**Figure 14.** Human calf muscle: a) anatomical T2 image; b) reconstructed conductivity shown on a [-3, 3] S/m scale. The dark ring surrounding the muscle area is due the low conductivity of the adipose tissue. The image artifacts bordering the tissue region are due to the attempt of reconstructing the surrounding air/space. This can be avoided by removing this area (through masking each image) and replacing it by pixels with a set zero conductivity.

*Observations related to this experiment:*

1) *There anatomical accuracy of the conductivity reconstructions and its overall relative homogeneity within the muscle areas appears to be at least as good as the T2 images (within the calf and excluding the image artifacts surround the calf). Specifically worth noting is the correct delineation of the gastrocnemius and soleus visible on the reconstructed conductivity map.*
2) *By setting a posteriori the value of the phase in the pixels containing surrounding space to zero the existence of the imaging artifacts (bands of high-low conductivity surrounding the tissue region) can be prevented (not shown here). This situation will not occur in the case of imaging ex-vivo prostates as they are immersed in fluid, or in in vivo scans where the FOV will fall inside the abdominal/pelvic region. Removing these artifacts will not be critical to assessing intraprostatic tissues, but will be useful to do once presenting these images to clinicians for review.*

***Task 2 Milestones:***

*Note that while the below tasks are complete, we expect to continue conducting phantom experiments over the course of the next year to continue to improve our image reconstruction algorithms and better understand any image artifacts that may appear in our clinical data acquisition.*

1. Validated MR-EPT algorithms **– Completed**
2. Fully functional protocol for obtaining MR-based images in a single serially acquired imaging session **– Completed**
3. 1 peer-reviewed publication submitted ***– in process, see Appendix # (TBC)***

**<u>Major Task 3: Submit documents for IRB and MRMC HRPO approval</u>**

a) Draft and submit IRB protocol revisions and new protocol submission

***Ex vivo Protocol:*** *Our Human Subjects Protocol was submitted to Dartmouth's IRB in November, after being approved by the Thayer School of Engineering, the Genitourinary (GU) Tumor Board, and the Norris Cotton Cancer Center's (NCCC) Clinical Cancer Research Committee (CCRC). This ex vivo component of this study was approved by the IRB on January 8th, 2014.*

***In Vivo Protocol:*** *We submitted a protocol modification request to the CCRC on July 16th, 2014, requesting approval to conduct the in vivo portion of the proposed work (to take place starting month 15 of this program); in consultation with our local IRB, we felt this staged approach was appropriate for this protocol. We expect this to be approved by CCRC within two weeks. Following CCRC approval it will be submitted to Dartmouth's IRB for approval (which should take 2-4 weeks) and then to MRMC HRPO for final review (which should take 2-4 weeks). This timeline keeps us on track to initiate our in vivo protocol by month 15 of this program.*

b) Draft and submit documentation for MRMC HRPO approval

***Ex vivo Protocol:*** *Our ex vivo Human Subjects Protocol was submitted to HRPO office on January 9th, 2014 and was approved by the HRPO on February 11th, 2014.*

**In Vivo Protocol:** *Once we have Dartmouth IRB approval for the in vivo protocol, we will submit all required modification documents to MRMC HRPO for review. We expect to do this within approximately 1 month.*

***Task 3 Milestones:***

1. Obtain IRB and MRMC HRPO approval for ex vivo and in vivo cohorts ***– ex vivo completed, in vivo in process (TBC)***

***SPECIFIC AIM 2: TO EVALUATE MR-EPT IN AN EX VIVO COHORT OF PROSTATES***

**Major Task 1: Optimize ex vivo MR-EPT and multi-parametric MR imaging**

a) Record MR-EPT and multi-parametric MR sequences of *ex vivo* prostates
*This task has been initiated. We have consented 10 men to participate in the ex vivo component of this study and have collected imaging data from 9 ex vivo prostates to date (1 man excluded due to the MRI not being available at time of surgery). We have developed a protocol to record this data while minimizing any MR artifacts associated with mounting the prostate in the bore of the MR scanner. The excised prostate is placed in an acrylic tub filled with deionized water (low conductivity). The prostate is supported and kept in place by two paper cylinder (similar to ex vivo muscle experiment shown in Figure 12). Minimal MR and MR-EPT artifacts associated with the mounting mechanism are visible.*

b) Optimize MR-EPT sequences and algorithms based on findings in this initial cohort
*Figures 15-17 show an example data set recorded from one of our first ex vivo cases and Figure 18 shows a more recent prostate case with multiple MR variants displayed.* ***These represent the first MR-EPT images ever created of an ex vivo human prostate.*** *To date, we have learned the following:*

1. *SE with 8 averages is currently optimal for ex vivo MR-EPT data acquisition.*
2. *The time to record an optimal MR-EPT sequence is approximately 30 minutes. This is still slightly long for clinical deployment, but for the purpose of this feasibility study we believe it is more important to acquire high quality MR-EPT data. If this is too long for in vivo data acquisition we will eliminate one of the other MR-variants (e.g. DCE-MRI or DW-MRI).*
3. *Our mounting mechanism produces minimal MR-EPT imaging artifacts.*
4. *There appears to be a dark region of low conductivity on the anterior surface of the prostate. This is likely due to the imaging artifacts discussed above.*

*Based on review of the images acquired at this stage, we have initiated the collection of our more formal data set for ex vivo evaluation using the SE (NSA=8) sequences for MR-EPT image acquisition (Task 2).*

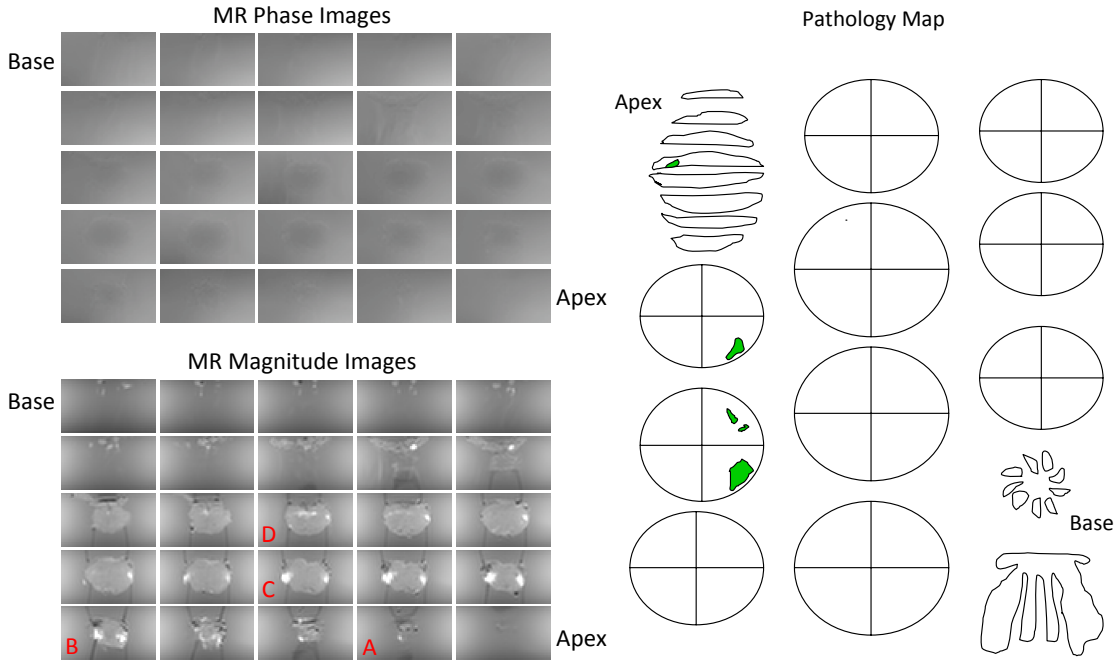


**Figure 15.** MR phase (top left) and magnitude (bottom left) images of an example ex vivo prostate case. Corresponding pathology map produced following microscopic evaluation of the specimen. Green islands in pathology map denote regions of tumor.

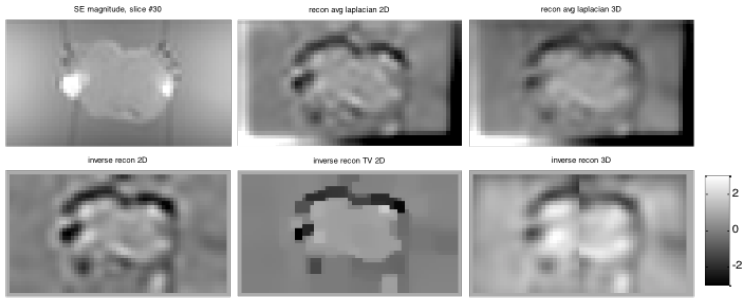


**Figure 16.** Magnitude image (SE) and conductivity reconstructions for an ex-vivo prostate case. A single slice is show for the various reconstruction algorithms being explored (Slice C in Fig #).

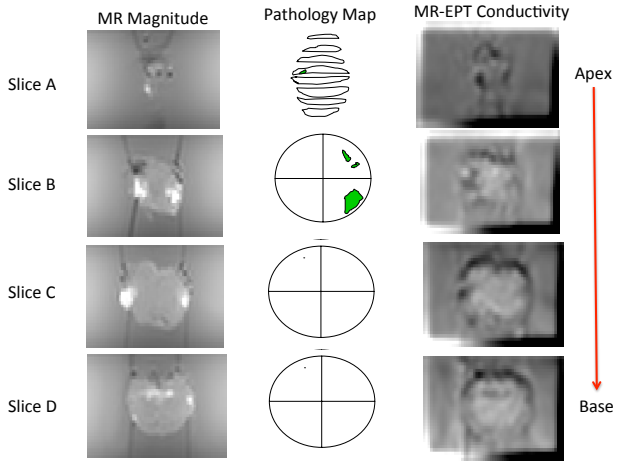


**Figure 17.** MR magnitude images, pathology maps, and the first ever produced MR-EPT conductivity images of an ex vivo prostate. The prostate shows well in the conductivity images. The dark region on the anterior prostate surface may be due to the imaging artifacts discussed above.

***Task 1 Milestones:***

1. Validation that our MR-EPT and multi-parametric MR protocol is initially optimized, robust, and repeatable – ***Completed***

**<u>Major Task 2: Evaluate *ex vivo* MR-EPT and multi-parametric MR imaging</u>**

a) Record multi-parametric MR sequences of ex vivo prostates

*We will be including the last 5 of the initial 9 prostate images (discussed above) as part of this cohort. We are actively recruiting patients to participate in this study and are currently imaging approximately 1 prostate per week. We are slightly behind schedule in this ex vivo cohort data acquisition. There are several reasons for this: 1) DHMC has been conducting fewer RALPs over the last year than in previous years (likely due to fewer men undergoing RALP nationally) and 2) the post-doctoral researcher working on*

*this program was unable to image prostates in the evening when some cases were finishing. We plan to do three things to mitigate this. First, we have identified a graduate student who is available in the evenings to image ex vivo prostates. He began doing this over the past month and is currently imaging approximately 1 ex vivo prostate per week. Second, we will be including the ex vivo data recorded from our in vivo cohort (we image both the men prior to undergoing RALP and their prostate once removed) in our final tally of ex vivo prostates. Thirdly, we will be requesting a modification to our original SOW to increase the length of the program by 6 months to accommodate the challenges we have had in recruitment. Finally, we have formed an early collaboration with colleagues at Yale University that we may be able to leverage to obtain additional ex vivo prostate MR-EPT images – this is a work in progress. Even if Yale is not able to provide ex vivo prostate data, we believe that we will hit our target of 50 prostates by the end of year 2 of this program at our current rate of recruitment.*

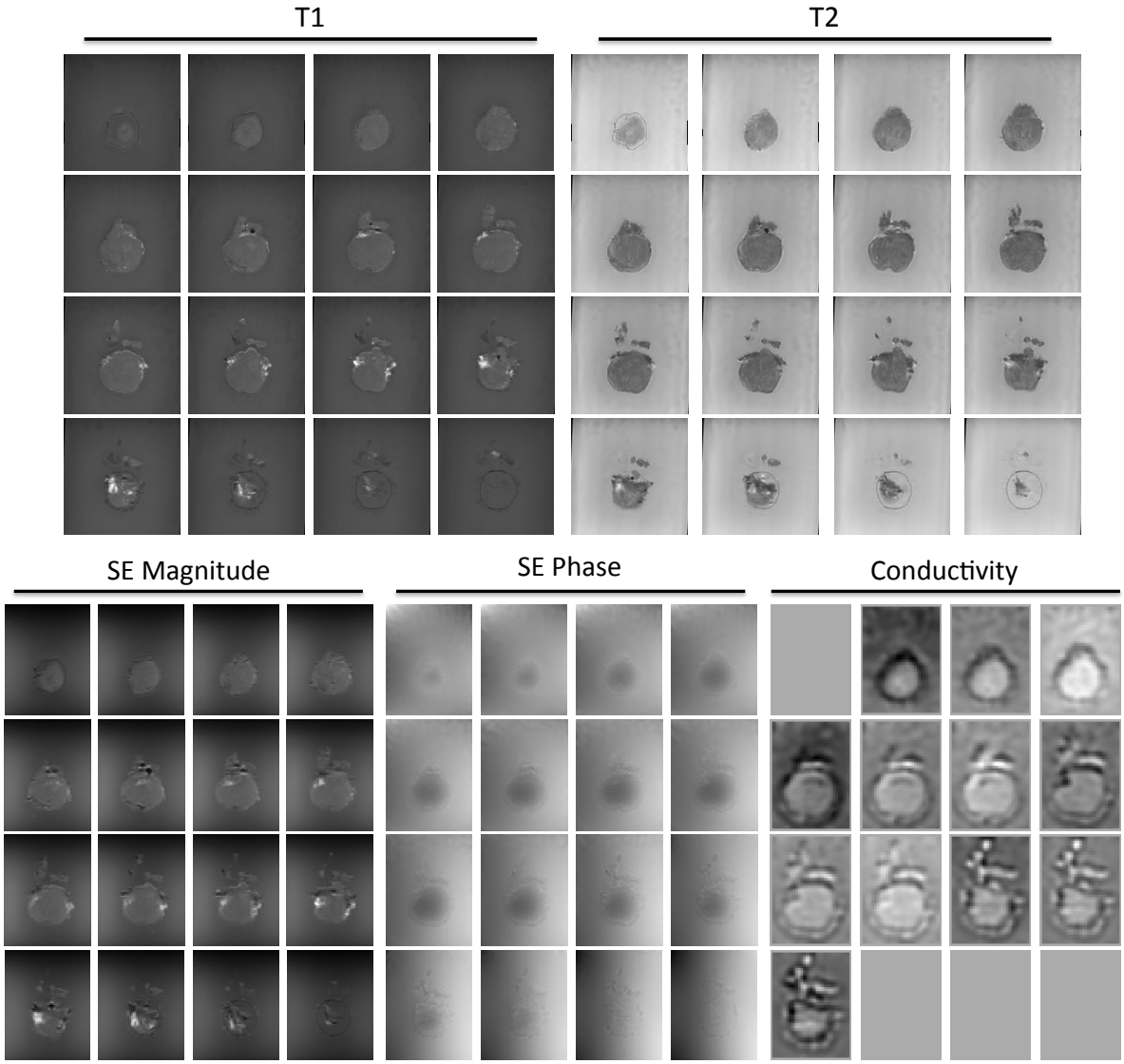


**Figure 18.** Example panel of MR images acquired from an ex vivo prostate scan. Panels for each data type (T1, T2, SE Magnitude, SE Phase, and Conductivity) represent cross-sectional images through an ex vivo prostate. Conductivity images clearly match the geometry of the T1, T2, and SE magnitude and phase images. These images will ultimately be compared with pathology maps as part of our data analysis.

b) Perform semi-quantitative and quantitative analysis of *ex vivo* prostate samples
*We have begun developing Matlab code to analyze our MR-EPT conductivity images, MR images (other variants), and pathology maps. Specifically, we are developing techniques to extract regions of interest from the MR-based images for comparison with the pathology maps. Mean values from these ROIs will be used as our metric for statistical analysis of the data.*

c) Statistically analyze MR-based images and pathological metrics
*This analysis has not formally begun to date, however we have begun dialogue with our biostatistician (Eugene Demidenko) and are convening in August to formalize and optimize this statistical analysis we aim*

*to use. We plan on having monthly meetings (with all collaborators over the next year) to discuss the clinical images and results to date to keep a constant monitoring of our progress.*

***Task 2 Milestones:***

1. Assessment of the clinical potential MR-EPT combined with multi-parametric MR might have for prostate imaging ***– in process (TBC)***
2. 1 peer-reviewed publication submitted ***– TBC***

***SPECIFIC AIM 3: TO EVALUATE MR-EPT IN AN IN VIVO COHORT OF PATIENTS***

**Major Task 1: Evaluate *in vivo* MR-EPT and multi-parametric MR imaging**

a) Record MR-EPT and multi-parametric MR sequences of *in vivo* and *ex vivo* prostates
*To be completed during Year 2 of this program*

b) Perform post-prostatectomy pathological assessment of extracted prostates
*To be completed during Year 2 of this program*

c) Statistically analyze MR-based images and pathological metrics
*To be completed during Year 2 of this program*

***Task 1 Milestones:***

1. Comparison between in vivo and ex vivo MR-EPT ***– TBC***
2. Preliminary clinical statistics defining utility of MR-EPT combined with other MR-imaging variants ***– TBC***
3. Initial parameter threshold values for use in detecting and staging prostate cancer ***– TBC***
4. 1 peer-reviewed publication submitted ***– TBC***

**KEY RESEARCH ACCOMPLISHMENTS**

- Built an MR-EPT Matlab-based toolbox for computing spatial distribution of conductivity and permittivity based on MR-phase images *using an inverse approach* to computing the electrical property distribution – 1st time this has ever been done.

- Developed and implemented advanced regularization schemes for improving MR-EPT images and incorporated these into our MR-EPT Matlab-based toolbox

- Confirmed that a surface flex-coil approach coupled with a spin echo sequence is sufficiently accurate for recording MR-EPT phase data for use in prostate conductivity imaging.

- Demonstrated significantly improved reconstructed electrical property images as compared to previous algorithms described in the literature through use of simulations and experimental validation.

- Produce the first ever MR-EPT-based conductivities of ex vivo human prostate.

**REPORTABLE OUTCOMES**

***Manuscripts***

Borsic A, Perreard I, Halter RJ, "An Inverse Problems Approach to MR-EPT Image Reconstruction," IEEE Transactions on Medical Imaging, to be submitted Summer 2014. ***(Appendix 1 - current draft)***

***Abstracts***

Borsic A, Perreard I, **Halter RJ**, "An inverse approach to MR-EPT reconstruction," Joint Annual Meeting ISMRM-ESMRMB 2014, May 2014. ***(Appendix 2 - abstract)***

Borsic A, Perreard I, Halter RJ, "MR-EPT Reconstruction Using an Inverse Formulation," XV. Conference on Electrical Impedance Tomography (EIT), Gananoque, Ontario, Canada, April 2014, April 2014. ***(Appendix 4 - abstract)***

***Presentations***
Borsic A, Perreard I, **Halter RJ**, "An inverse approach to MR-EPT reconstruction," Joint Annual Meeting ISMRM-ESMRMB 2014, May 2014. ***(Appendix 3 - poster)***

Borsic A, Perreard I, Halter RJ, "MR-EPT Reconstruction Using an Inverse Formulation," XV. Conference on Electrical Impedance Tomography (EIT), Gananoque, Ontario, Canada, April 2014, April 2014. ***(Appendix 5 - presentation)***

**CONCLUSION**
It is a daily challenge for clinicians to determine whether a man recently diagnosed with prostate cancer has aggressive disease requiring immediately radical therapy or indolent disease requiring a more passive watchful waiting or active surveillance approach. This program is focused on developing Magnetic Resonance – Electrical Property Tomography (MR-EPT) specifically for prostate imaging. Over the past year we have developed a new MR-EPT algorithm that is based on an inverse problem approach to estimate the prostate's electrical conductivity given magnetic field phase and magnitude images acquired using custom MR sequences. We have determined an optimal pulse sequence (based on a spin echo approach) that enables sufficient resolution and accuracy, while being able to be acquired in a timely manner. A number of complex phantom experiments have been used to demonstrate the capabilities of MR-EPT with a focus on evaluating the approach for prostate imaging. Finally, the first ever ex vivo prostate conductivity images were generated using MR-EPT. Over the course of the next year, we will be focusing primarily on clinical data acquisition (both ex vivo and in vivo cohorts) and in analyzing images acquired to assess the potential of using MR-EPT (coupled with other MR imaging variants) to distinguish between aggressive and indolent prostate cancer.

**REFERENCES**


1. Halter RJ, Hartov A, Heaney J, Schned A, Paulsen KD, 'Electrical Impedance of the Human Prostate', IEEE Transactions on Biomedical Engineering, 54(7):1321-1327, 2007.
2. Halter RJ, Schned AR, Heaney JA, Hartov A, Schutz S, Paulsen KD, 'Electrical impedance spectroscopy of benign and malignant prostatic tissues,' Journal of Urology, 179(4):1580-1586, 2008.
3. Halter RJ, Hartov A, Paulsen KD, Schned A, Heaney J 'Genetic and least squares algorithms for estimating spectral EIS parameters of prostatic tissues,' Physiological Measurement, 29: S111-S123, 2008.
4. Halter RJ, Schned AR, Heaney JA, Hartov A, Paulsen KD, 'Electrical properties of prostatic tissues: I. single frequency admittivity properties,' Journal of Urology, 182:1600-1607, 2009.
5. Halter RJ, Schned AR, Heaney JA, Hartov A, Paulsen KD, 'Electrical properties of prostatic tissues: II. Spectral admittivity properties,' Journal of Urology, 182:1608-1613, 2009.
6. Halter RJ, Schned AR, Heaney JA, Hartov A, "Passive bioelectrical properties for assessing high- and low-grade prostate adenocarcinoma," The Prostate, 71:1759-1767, 2011.
7. Halter RJ, Hartov A, Paulsen KD, 'Experimental justification for using 3D conductivity reconstructions in electrical impedance tomography,' Physiological Measurement, 28:S115-S127, 2007.
8. Halter RJ, Hartov A, Paulsen KD, 'A broadband high frequency electrical impedance tomography system for breast imaging,' IEEE Transactions on Biomedical Engineering, 55(2):650-659, 2008.
9. Borsic A, Halter RJ, Wan Y, Hartov A, Paulsen KD 'Sensitivity Study and Optimization for a 3D Electric Impedance Tomography Prostate Probe,' Physiological Measurement, 30:S1-S18, 2009.
10. Borsic A, Halter RJ, Wan Y, Hartov A, Paulsen KD, 'Electrical impedance tomography reconstruction for three dimensional imaging of the prostate,' Physiological Measurement, 31:S1, 2010.
11. Wan Y, Halter RJ, Borsic A, Manwaring P, Hartov A, Paulsen KD, 'Sensitivity of an ultrasound coupled transrectal electrical impedance tomography system for prostate imaging,' Physiological Measurement, 31:S17, 2010.
12. A. Borsic, W. Lionheart, C. McLeod: Generation of anisotropic regularization filters for Electrical Impedance Tomography. IEEE Trans. on Medical Imaging, 21, 579-587, 2002.
13. H. Syed, A. Borsic, A. Hartov, RJ Halter - Anatomically accurate hard priors for Transrectal Electrical Impedance Tomography (TREIT) of the prostate. Physiological Measurement, 33, 719-738, 2012.
14. A. Borsic, C. McLeod, W. Lionheart, N. Kerrouche: Realistic 2D human thorax modeling for Electrical Impedance Tomography. Physiological Measurement, 22, 77-83, 2001.
15. U. Katscher, D.H. Kim, and J.K. Seo, "Recent Progress and Future Challenges in MR Electric Properties Tomography". Computational and Mathematical Methods in Medicine, vol. 2013, Article ID 546562

**APPENDICES**
**Appendix 1: IEEE TMI Draft**
**Appendix 2: ISMRM Abstract**
**Appendix 3: ISMRM Poster**
**Appendix 4: EIT Conference Abstract**
**Appendix 5: EIT Conference Presentation**

# An Inverse Problems Approach to MR-EPT Image Reconstruction

A. Borsic, I. Perreard, R. J. Halter

***Abstract*—We show**

*Keywords*: Electrical Properties Tomography, Magnetic Resonance, Inverse Problem, Regularization, Total Variation, Primal Dual Interior Point Method

## I. Introduction

Magnetic Resonance Electrical Properties Tomography (MR-EPT) is a novel approach to imaging electrical conductivity and permittivity by Magnetic Resonance Imaging (MRI). MR-EPT is based on mapping B1 field amplitude and phase information. The B1 field is the Radio Frequency (RF) field at the Larmor's frequency used in MR imaging for flipping the magnetic moments of the protons. This field, emitted by an RF coil, propagates in the bore of the scanner and interacts with the body / phantom being imaged. This interaction can be generally described by the Helmholtz equation. In 1991 Haake *et.al.* [REF] noted that electrical conductivity and permittivity of the body / phantom being imaged influence the amplitude and phase of the B1 field, and that it was possible to fit B1 field information to recover the conductivity / permittivity of layered structures. B1 amplitude / phase was considered along a spatial line perpendicular to the layers and a 1D analytical model was fitted to the data to recover the electrical properties of each layer in the model. In 2009 an imaging approach was proposed by Katscher *et.al.*, where, under certain approximations, conductivity was shown to be proportional to the Laplacian of the B1 phase and permittivity to be proportional to the Laplacian of the B1 amplitude. As this relationship holds point-by-point it can be used in principle to reconstruct a 3D electrical properties image of the object under investigation. Being the differentiation process highly sensitive to noise, this approach is not practical and Katscher *et.al.* used the Gauss theorem to turn lower the differentiation order to one: they show that conductivity and permittivity are proportional to surface integrals of the gradient of B1 phase and amplitude, over the surface of an arbitrary block of pixels where the electrical properties are summed to be more or less constant. In practice this approach is used for integrating gradients of B1 gradients of phase and amplitude over the surface of blocks of, for example, 3×3×3, or 5×5×5 [REf and verify] pixels to yield the conductivity / permittivity of that volume.

In alternative to the previous approaches to MR-EPT image reconstruction we propose a novel approach based on an inverse problem formulation. In this approach pixels of the reconstructed image (conductivity or permittivity) are taken as parameters to be fitted. For this approach we develop a forward model, linking parameters to the B1 data. The forward model allows predicting the expected B1 data corresponding to the parameters, and comparison to measured B1 data. We derive the Jacobian matrix of the forward model, which is used for updating the model parameters. Finally we adopt an inverse formulation with regularization, which stabilizes the inversion.

Overall the proposed approach has two general advantages. The first advantage is that no spatial differentiation is needed for the B1 data. In previous approaches conductivity / permittivity is computed in a point-by-point fashion from B1 data with local formulations that involve first or second derivatives. With an inverse problem approach only comparison between model and measured B1 data is needed, and no differentiation avoiding thus a noise sensitive process. The second advantage is that the resolution of the reconstructed image is determined by the regularization term. We show, for example, that using Total Variation regularization results in the ability to reconstruct very sharp profiles. In biomedical imaging applications there would be the opportunity of incorporating prior information from MRI structural images [REFS] which would be readily available, enhancing the application of this technique in-vivo. One drawback of the solution we propose is that it is computationally more expensive then previous approaches. We discuss however how to subdivide an image and how to process the resulting subdomains separately, reducing the computational complexity. [layout organization of paper]

to do: metion paper by Han Wen as usign 2nd derivatives and as being first imaging approach to do: mention MREIT ?

## II. Direct Reconstruction Approaches

DISCUSSION on what's measurable in MREPT.

The B1 field set by the scanner can be described by the Helmholtz equation [REF Wen, and Ulrich review]:

$$\nabla^2 \vec{B1} = -\mu\omega^2 k \vec{B1} + \left[\frac{\nabla}{k} \times (\nabla \times \vec{B1})\right] \qquad (1)$$

where $k = \epsilon - j(\sigma/\omega)$, and $\omega$ is the angular frequency of the $\vec{B1}$ field; where $\sigma$ is the electrical conductivity, $\epsilon$ the electrical permittivity, and $\mu$ the magnetic permeability. Assuming now that the conductivity / permittivity / permeability distribution is piecewise constant ($\nabla k = 0$) or slowly varying ($\nabla k \approx 0$), and that $k$ is isotropic, the *central* MR-EPT equation can be


A. Borsic is with the Thayer School of Engineering, Dartmouth College, NH, USA, email: Andrea.Borsic@Dartmouth.edu. I. Perreard is with the Department of Radiology, Dartmouth Hitchcock Medical Center, Dartmouth College, NH, USA. R. J. Halter is with the Thayer School of Engineering, Dartmouth College, NH, USA

derived [Ref Haake, Wen, U Review]: (SAY mu is constant in tissues)(NOTE: ref to paper by Korens on the gradient term)

$$k = \frac{-1}{\mu\omega^2}\frac{\nabla^2\vec{B1}}{\vec{B1}} \tag{2}$$

where $k$ is the complex permittivity point-by-point in space expressed as a function of the B1 field. Separating now the real and imaginary parts in (2) one obtains:

$$\sigma = \frac{1}{\mu\omega}\ \mathrm{Im}\left[\frac{\nabla^2\vec{B1}}{\vec{B1}}\right] \tag{3}$$

and

$$\epsilon = \frac{-1}{\mu\omega^2}\ \mathrm{Re}\left[\frac{\nabla^2\vec{B1}}{\vec{B1}}\right] \tag{4}$$

Despite the simplificative assumptions made in deriving (2), (3), (4), these have been shown in [REF Haake] to allow successful fitting layered models and in [REF Wen] to result in successful imaging of electrical properties in phantoms and in-vivo. In order to use (3) and (4) both the magnitude and phase of B1 need to be mapped. Wen [REF] noted that $\sigma$ is mostly affected by B1 phase and that $\epsilon$ is mostly affected by B1 amplitude, suggesting that $\sigma$ or $\epsilon$ could be reconstructed separately from amplitude or phase information, with small errors, as

$$\sigma \approx \frac{1}{\mu\omega}\nabla^2\phi(\vec{B1}) \tag{5}$$

and

$$\epsilon \approx \frac{-1}{\mu\omega^2}\nabla^2|\vec{B1}| \tag{6}$$

The validity of this further approximation has been studied in [REF Voigt, paper 11 of review], showing that for physiological values of $\sigma$ and $\epsilon$ the maximum quantitative error is in the order of 10%, and that conductivities are overestimated and permittivity underestimated. Nevertheless this further approximation is particularly useful for practical purposes, as if one is interested in only one of the two quantities, $\sigma$ or $\epsilon$, that single quantity can be recovered from a B1 single mapping sequence, for phase or for amplitude, respectively.

As shown in [Ref Wen] (3), (4), (5), (6) are highly sensitive to noise. A systematic approach to imaging $\sigma$ and $\epsilon$ was developed in [Ref Katscher 2009], and the issue of noise sensitivity was addressed by using the Gauss theorem to reduce the order of differentiation to one.

## III. Forward Problem

A relationship that links the B1 field data to the electrical conductivity $\sigma$ and permittivity $\epsilon$ constitutes a forward model, describing how the measured data can be predicted from the spatial distribution of $\sigma$ and $\epsilon$. A forward model allows fitting predicted data to the measured data by acting on the spatial distribution of $\sigma$ and $\epsilon$. Particularly we derive a forward model from (5), (6). Indicating with $\phi$ the mapped phase $\phi(\vec{B1})$ and with $\Lambda$ the mapped amplitude $|\vec{B1}|$, we obtain

$$\nabla^2\phi = \mu\omega\sigma \tag{7}$$

and

$$\nabla^2\Lambda = \mu\omega^2\epsilon \tag{8}$$

Therefore both $\phi$ and $\Lambda$ can be described by the Poisson equation, under the common MR-EPT approximations. As the relationships between $\phi$ and $\sigma$ expressed by (7), and between $\Lambda$ and $\epsilon$ by (8) are identical, with exception of the factor $\omega$ in the first and $\omega^2$ in the second, we focus here, for brevity, only on reconstruction of $\sigma$, as identical methods apply to the reconstruction of $\epsilon$.

Boundary conditions appropriate to the problem at hand need to be used for solving (7). As we attempt to match a measured phase $\phi_{meas}$ with (7), we adopt Dirichlet conditions on the boundary

$$\phi(r) = \phi(r)_{meas} \quad \forall r \in \partial\Omega \tag{9}$$

where $r$ is a point in space and $\Omega$ is the boundary of the imaging domain. Therefore $\phi_{meas}$ is perfectly matched at the boundary, by using (9), and it will be matched point-by-point inside the domain, as we discuss later, by acting on $\sigma$. It is worth noting that for any value of measured data $\phi_{meas}$ the condition (9) is compatible with (7) [REF], and therefore a solution to (7) always exists for those boundary conditions, and it is worth noting that such a solution is unique [REF]. We call therefore (7) and (9) a forward model for MR-EPT, and the solution of this model exists and is unique.

## IV. Inverse Formulation

Having a forward model linking $\phi$ to $\sigma$, it can be used to fit $\phi_{meas}$, for example, in the least squares sense as

$$\sigma_{rec} = \mathrm{argmin}\|\phi(\sigma) - \phi_{meas}\|^2 \tag{10}$$

where $\sigma_{rec}$ is the electrical conductivity spatial distribution reconstructed by fitting $\phi(\sigma)$ to the measured phase $\phi_{meas}$. This fitting is accomplished by acting on $\sigma$, and in the above equation we have explicitly indicated the dependence of the model predicted phase $\phi$ on $\sigma$.

As phase measurements are noisy we adopt a regularization term [REF], which stabilizes the inversion, transforming (10) in

$$\sigma_{rec} = \mathrm{argmin}\|\phi(\sigma) - \phi_{meas}\|^2 + \alpha\Psi(\sigma) \tag{11}$$

where $\alpha$ is scalar value, the Tikhonov value, that controls the amount of regularization, and where $\Psi(\sigma)$ is a regularization functional. These functionals are often quadratic and involve first or second differential operator [REFs], we defer the discussion on the form of the regularization functional, as we will show two different ones, and we will discuss the opportunity of using others, that incorporate prior structural information.

## V. Implementation

(Talk about effect of regularization and say we will have two implementations)

In order to implement an MR-EPT reconstruction based on (11) a regularization functional needs to be defined, a numeric method for computing $\phi(\sigma)$ as defined by (7) and (9) must be implemented, and the Jacobian matrix of $\phi(\sigma)$ needs to be computed.

### A. Quadratic Regularization

In a first implementation example we use a classical quadratic functional, writing (11) as

$$\sigma_{rec} = \text{argmin}\|\phi(\sigma) - \phi_{meas}\|^2 + \alpha\|L\sigma\|^2 \qquad (12)$$

where we have discretized now $\sigma$ on the same pixel grid as used by the MR scanner to map $\phi_{meas}$, and therefore $\sigma$ is now a finite vector of discretized values. The matrix $L$ is a regularization matrix, which we have chosen to be the Laplacian of the conductivity distribution, a relatively common choice [REF].

Applying the Newton-Raphson method to (12) an update equation for the conductivity can be derived as

$$\delta\sigma = -\left[J^T J + \alpha L^T L\right]^{-1} \left[J^T(\phi(\sigma) - \phi_{meas}) - \alpha L^T L(\sigma - \sigma^*)\right] \qquad (13)$$

where $J$ is the Jacobian matrix of the forward operator $\phi(\sigma)$, and $\sigma^*$ is the starting conductivity distribution. The above formula can be used starting from an initial conductivity $\sigma^*$, for example a unform distribution, and than by updating this initial estimate as $\sigma_{rec} = \sigma^* + \delta\sigma$. A single update is sufficient as the forward model is linear in $\sigma$ and therefore the Newton-Raphson method finds the solution to (12) in one step. In order apply (13) one has to compute $\phi(\sigma)$ and the Jacobian matrix $J$.

The forward problem $\sigma \rightarrow \phi(\sigma)$ in three dimensions consists in solving

$$\frac{\partial^2\phi}{\partial x^2} + \frac{\partial^2\phi}{\partial y^2} + \frac{\partial^2\phi}{\partial z^2} = \mu\omega\sigma \qquad (14)$$

where the $(x, y, x)$ are the coordinates in the axes $(\vec{x}, \vec{y}, \vec{z})$, which we take to be aligned to the main axes of the image stack. The Partial Differential Equation (14) can be easily discretized on the image grid using Finite Difference schemes [REF] expressing the partial derivatives as

$$\frac{\partial^2\phi}{\partial x^2} = \frac{\phi(x + h_x) - 2\phi(x) + \phi(x - h_x)}{h_x^2} \qquad (15a)$$

$$\frac{\partial^2\phi}{\partial y^2} = \frac{\phi(y + h_y) - 2\phi(y) + \phi(y - h_y)}{h_y^2} \qquad (15b)$$

$$\frac{\partial^2\phi}{\partial z^2} = \frac{\phi(z + h_z) - 2\phi(z) + \phi(z - h_z)}{h_z^2} \qquad (15c)$$

where $h_x, h_y, h_z$ are respectively the pixel spacings along $(\vec{x}, \vec{y}, \vec{z})$, and where the points $(x - h_x), x, (x + h_x), (y - h_y), y, (x + h_y), (z - h_z), z, (z + z_x)$ translate into indices into the vector of discrete phase values $\phi$ which is sought out. As standard in Finite Differences, the partial differential equation (14) is turned into a linear system

$$A\phi = b \qquad (16)$$

where $A$ is a matrix deriving from the application of (15) to the different pixels in the image, $b$ is a right hand side (RHS) deriving from the evaluation of the term $\mu\omega\sigma$ in (14) at each pixel location in the image, and where $\phi$ is the vector of computed phase values.

In turning (15) into (16) boundary conditions need to be accounted for, which can be done as follows

- for all the pixels on the boundary surface of the image stack we write 1 on the diagonal element $A(i, i)$, where $i$ is the index of each of these pixels, and we write $b(i) = \phi(i)_{meas}$. This sets those pixel values to the Dirichlet condition.
- for all the pixels that are internal to the domain - defined by being at least 1 pixel away from the boundary, we apply (15), and compute the RHS as $b(i) = \mu\omega\ \sigma(i)$, where $i$ the the index of the considered pixel.

Solving now the linear system (16) results in the vector $\phi$ of computed phase values.

A similar approach is used for building the matrix $L$, which is a Laplacian operator. The purpose of $L$ is to limit too fast spatial variations in the image, which arise typically from noise in the data. The term $\|L\sigma\|^2$ takes large values corresponding to fast variations in $\sigma$, penalizing them therefore in (12). In order to build $L$ we use in the interior of the domain the same finite differences used for solving the forward problem (15). As boundary conditions we use mirroring boundary conditions [REF?], where, for example, if the term $(x + h_x)$ in (15a) falls outside the domain, we assume $(x + h_x) = (x - h_x)$ and write the second derivative, for that image location, as

$$\frac{\partial^2\phi}{\partial x^2} = \frac{-2\phi(x) + 2\phi(x - h_x)}{h_x^2} \qquad (17)$$

and similar conditions are used for derivatives in $y$ and $z$.

The Jacobian matrix in (12) can be computed from (16) using the following matrix identities

$$J = \frac{\partial\phi}{\partial\sigma} = \frac{\partial(A^{-1}b)}{\partial\sigma} = A^{-1}\frac{\partial b}{\partial\sigma} = A^{-1}\xi \qquad (18)$$

where $\xi$ is the derivative of $b$ with respect to $\sigma$, and therefore $\xi(i) = 0$ for all indices $i$ corresponding to pixels on the boundary (for which the Dirichlet condition has been set), and $\xi(i) = \mu\omega$ for all the indexes corresponding to pixels in the interior of the domain, where $b(i)$ is set to $b(i) = \mu\omega\sigma(i)$. Equations (16) and (18) allow therefore to compute $\phi$ and $J$, which are in turn used in 13 to produce $\sigma_{rec}$.

As we will show this procedure produces in successful reconstructions on synthetic and true data. The use of a quadratic regularization functional as in (13) results in smoother reconstructed conductivity profiles. The benefit of the formulation (11) is that different terms can be used for regularization. In the next subsection we will discuss briefly the use of Total Variation as a regularization term, and we will later compare results from the two inverse formulations we propose to direct MR-EPT reconstruction approaches.

### B. Total Variation Regularization

In the previous sections we have developed a framework for MR-EPT image reconstruction based on inverse problems. One benefit of this framework is that different regularization terms can be chosen. Regularization functional affect how the reconstructed image is smoothed and different choice

are appropriate for different situations. In this subsection we propose using Total Variation (TV) as a regularization functional in (11). TV is a relatively novel form of regularization that results in sharper reconstructions compared to quadratic regularization terms, as in 13. As the reconstruction of sharp image transitions is challenging in MR-EPT, the use of TV regularization provides the opportunity of reconstructing more faithfully fast spatial variations.

The TV functional is defined as $TV(\sigma) = \int_\Omega |\nabla(\sigma)| d\Omega$, where $\Omega$ is the imaging domain. The inverse formulation (11) becomes therefore

$$\sigma_{rec} = \text{argmin} \|\phi(\sigma) - \phi_{meas}\|^2 + \alpha \; TV(\sigma) \qquad (19)$$

TV is understood to result in shaper reconstructions, as, for example, for step changes the TV functional remains finite, while quadratic functionals like $\int_\Omega |\nabla(\sigma)|^2 d\Omega$, or, $\int_\Omega |\nabla^2(\sigma)|^2 d\Omega$, which are common quadratic regularization functionals, go to infinity. Quadratic functionals take therefore larger (or infinite) values corresponding to fast spatial changes in the conductivity distribution, rendering the reconstructions smoother. We refer the reader to [REF Rudin][REf Chan?][REF Borsic] for detailed discussion of the TV functional properties.

While the use of TV is desirable for the reconstruction of sharp variations, the image reconstruction expressed by (19) is a non-differentiable optimization problem, and special techniques need to be employed to minimize $\|\phi(\sigma) - \phi_{meas}\|^2 + \alpha \; TV(\sigma)$ acting on $\sigma$. For the sake of brevity we do not report specific details, but we adopt the Primal Dual - Interior Point framework developed in [REF Borsic] for optimizing (19), and specifically the algorithm named "PD-IPM - L1-L2 Norm" whose pseudo code is reported in the cited manuscript. The MR-EPT forward model $\phi(\sigma)$ and Jacobian matrix $J$ developed in the previous section V-A are plugged in into the optimization algorithm, resulting in $\sigma_{rec}$ as in (19).

## VI. Numerical Experiments

In order to validate the approach above we have conducted a few numerical experiments which are presented in this section. In these experiments we have focused on conductivity reconstruction, but an approach for permittivity reconstruction would be basically identical given the similarity of (5) and (6). To this end we have setup a simulation where a cubic block of 20x20x20 mm is split in two parts with a plane passing in the middle. One part of the block is set to have a conductivity of 1 $\text{Sm}^{-1}$ and the other part of 2 $\text{Sm}^{-1}$, as shown in Figure 1. The block presents therefore a sharp conductivity change at the interface between these two parts.

The simulated cube was discretized with Finite Differences with a resolution of $1 \times 1 \times 1$ mm, and the MRI phase was computed using equations (14) to (16). A Dirichlet boundary condition of $\phi(r) = 0 \quad \forall r \in \partial\Omega$ was assumed on the boundary. As discussed in Section III Dirichlet boundary conditions can be used for matching a measured phase at the boundary of the domain in forward solving. In the absence of boundary data the condition $\phi(r) = 0 \quad \forall r \in \partial\Omega$ is a practical condition that is compatible with the Poisson equation and that allows determining a unique solution. This choice does not alter the reconstructed conductivity, which depends on the Laplacian of the solution - the value of which is enforced within the domain by the Poisson equation itself.

A Gaussian noise with 2.5% standard deviation was added to the computed phase, producing a signal to noise ratio that is representative of the data acquired in actual MRI experiments (REF?). Figure 7 shows a 2D cross section of the synthetic phase with and without noise. As it is possible to notice, the curvature / Laplacian of the phase is more pronounced in the left part of the domain, as the conductivity in this region presents a higher value, and from (5) the Laplacian will therefore take a larger value.

The phase data was fed into three different reconstruction algorithms. The first is based on the direct approach proposed by Katscher *et. al.* in [**?**]. This algorithm is based on (2) and on using an integration volume, which allows in turn to apply the Gauss theorem and convert the volume integral of (2) to a surface integral which has only first derivatives of the field variables [**?**]. This is a direct approach in the fact that the output conductivity is computed directly from the input phase by taking derivatives and by integration of derivatives on integration volumes. In our own implementation of this algorithm was used an integration volume of $5 \times 5 \times 5$ pixels and we have estimated phase derivatives using SavitzkyGolay [**?**] filters involving 3 points. Katscher *et. al.* uses similar integration volumes, but 5 to 9 points for derivatives estimation. In this particular dataset we found that using only 3 points results in probably a good compromise between image sharpness and noise sensitivity. A second and third algorithms are based on the proposed inverse formulation approach, respectively with quadratic regularization as in (12) and with TV regularization as in (19).

Reconstructions for the three different algorithms are shown in Figure 3 using a fixed gray-scale for all figures spanning the values of 0.5 to 2 $\text{Sm}^{-1}$. The direct algorithm successfully reconstructs the phase information, showing a higher conductivity on the left side of the domain, and a vertical splitting line between the more conductivity and less conductive regions. A darker band is present at the boundary if the image as a border of 2 pixels in needed for setting up the integration volumes of 5 pixels (central pixel plus 2 pixels per side). The inverse quadratic algorithm also successfully reconstructs the conductivity profile showing a more conducting and a less conducting region respectively on the left and right regions of the image. This algorithm shows similar smoothness compared to the direct algorithm, describing the transition between the two conductivities as a smooth transition. Total Variation reconstruction show a particularly good identification of the conductivity transition, showing a sharp change in the conductivity distribution, resulting in better overall estimation of the the original data as TV is an appropriate image prior for distributions with sharp transitions like the one used for these tests. The images produced by the inverse approach present a border of one pixel. Pixels on the boundary are not estimated as they can be affected by the boundary condition $\phi(r) = 0$.

Figure (4) shows plots of the conductivity values along a line of pixels crossing the dataset from left to right. Figure (4A NOTE ADD SUBCAPTION) shows the original conductivity

profile used for generating synthetic phase data. Figures (**??**) show reconstructions for the three different algorithms in bold line, with superimposed in dotted line the original conductivity profile. While subtle differences exist between the direct approach and the inverse approach with quadratic regularization, the reconstruction with TV regularization is a rather faithful reconstruction of the original profile. The inverse approach allows therefore to select regularization functionals that are appropriate for the problem at hand. Besides TV and similar edge-preserving techniques it is possible to envision using ad-hoc functional that incorporate prior structural information as, for example, in [].

Lastly, Figure 6 shows the fitting processes the reconstruction algorithm. The dark bold line represents the phase values for a 1D line of pixels across the dataset, from left to right. This line values form approximately a parabolic shape, but with two different curvatures, as pixels on the line span the two conductivity regions. This line is also somewhat irregular as affected by noise. The thin dotted line represents the initial synthetic phase, computed for a homogeneous conductivity distribution, which is the stating guess of the inversion. The dash–dotted line represents instead the final fit of the algorithm, resulting from forward solving after the conductivity has been updated with (13). This figure demonstrates therefore the convergence of the algorithm, and how, without differentiation, it is possible to base MR-EPT reconstruction on an algorithm that will fit the phase data. In the presence of noise, this fitting can be stabilized with regularization techniques, which allow fitting the general trend of the phase, but not the small artifacts caused by noise, as shown by Figure 6.

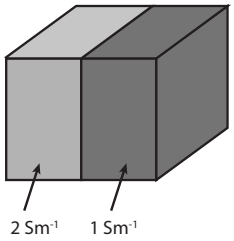


Fig. 1. Setup used for the numerical experiment: a cube of 20×20×20 mm has been setup to have a conductivity of 1 $\mathrm{Sm}^{-1}$ on one side and of 2 $\mathrm{Sm}^{-1}$ on the other. MRI phase on this cube has been computed for a 3T magnet using REF

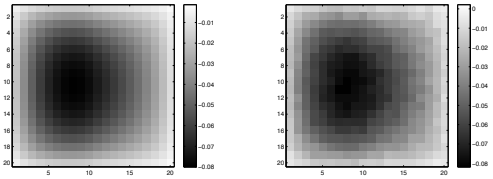

Fig. 2. 2D cross section in the horizontal plane of the 3D computed MRI phase for the conductivity setup shown in Figure 1. As expected the computed phase has a higher curvature corresponding to the more conductive region, as here the Laplacian takes a larger value compared to the less conducting region. The units used for plotting the phase are radians, and the range is -0.08 to 0.00 radians. ADD COMMENTS for noisy phase.

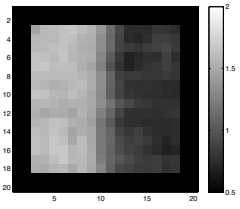

color

Fig. 3. Caption TBD.

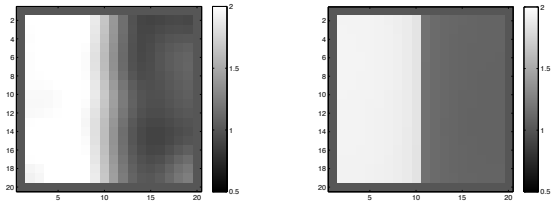

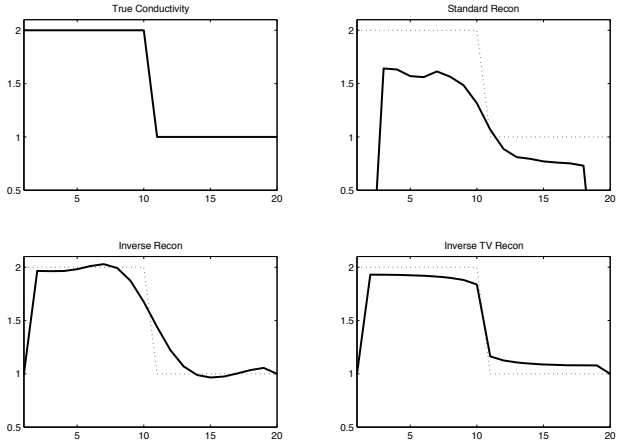


Fig. 4. Caption TBD.

Fig. 5. Caption TBD.

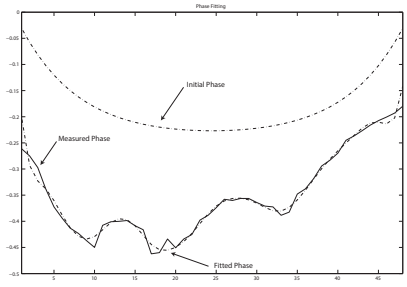


Fig. 6. Caption TBD.

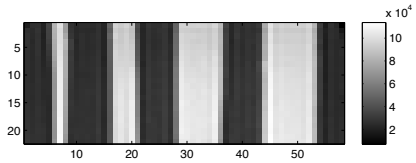


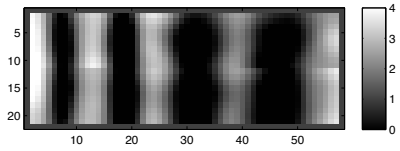

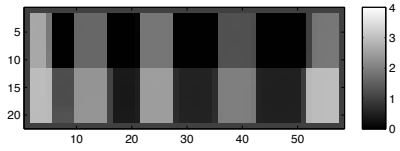

Fig. 7. 2D cross section in the horizontal plane of the 3D computed MRI phase for the conductivity setup shown in Figure 1. As expected the computed phase has a higher curvature corresponding to the more conductive region, as here the Laplacian takes a larger value compared to the less conducting region. The units used for plotting the phase are radians, and the range is -0.08 to 0.00 radians. ADD COMMENTS for noisy phase.

5571

# An Inverse Approach to MR-EPT Reconstruction

Andrea Borsic[1], Irina Perreard[2], and Ryan J Halter[1]

[1]*Thayer School of Engineering, Dartmouth College, Hanover, NH, United States,* [2]*Radiology Department, Dartmouth College, Hanover, NH, United States*

**Purpose:** We present a novel approach to imaging an organ's electrical properties with MRI using a variant of the recently developed MR Electrical Properties Tomography (MR-EPT). MR-EPT makes certain simplifications to the Maxwell Equations describing the propagation of the B1 RF field; in particular, the electrical conductivity is shown to be proportional to the Laplacian of the B1 field phase (Eq. 1). Computing the Laplacian (second derivatives) of the phase is extremely sensitive to noise and undesirable. A recent approach using Gauss' theorem to express conductivity as a surface integral of the gradients of B1 phase, reduces this computation to a first order derivative and makes image reconstruction less sensitive to noise. However, even in this case noisy MR data can limit reconstruction quality. Here, we propose an inverse formulation, in which the spatial distribution of conductivity is taken as a parameter to be fitted; specifically, a simulated phase is computed from an initial estimate of the conductivity distribution and fitted to the MR measured B1 phase. This has the advantage of not requiring computation of any phase derivatives. This approach is applicable to both MR-EPT conductivity and permittivity imaging, and has the potential of improving MR-EPT in in-vivo applications.

**Methods:** MR-EPT conductivity imaging is based on Eq. (1), where the conductivity, $\sigma$, is approximately proportional to the Laplacian of the phase of the transmit B1 field $\phi(H^+(r))$ at any point in space, $r$. Conversely, given a spatial distribution of $\sigma$, it is possible to express the resulting phase as Eq. (2), where a simulated phase $\phi_{sim}$ is computed from $\sigma(r)$ by solving the Poisson equation.

**Eq. 1:** $$\sigma(r) \approx \frac{1}{\omega\mu}\nabla^2\phi(H^+(r))$$

**Eq. 2:** $$\nabla^2(\phi_{sim}) = \omega\mu\sigma(r)$$

Reconstruction of $\sigma(r)$ is therefore based on: 1) taking an initial estimate of $\sigma(r)$, for example a uniform distribution, 2) computing the corresponding simulated phase $\phi_{sim}$ by solving Eq. (2), and 3) updating $\sigma(r)$ based on the discrepancy between the measured and simulated phases $\| \phi(H^+) - \phi_{sim} \|^2$, in the least squares sense. This approach is known as an inverse formulation, and the update of $\sigma$ can be expressed using Eq. (3), where $J$ is the Jacobian of the conductivity to phase mapping expressed by Eq. 2, $L$ is a regularization matrix, and $\alpha$ is a regularization parameter used to stabilize the inversion. The initial or current conductivity distribution is iteratively updated as $\sigma_{new} = \sigma_{cur} + \delta\sigma$, where $\sigma_{cur}$ is the current estimate of $\sigma(r)$. Since the problem linear, a single iteration of Eq. 3 results in the sought conductivity.

**Eq. 3:** $$\delta\sigma = (J^T J + \alpha L^T L)^{-1}(J^T(\phi(H^+(r)) - \phi_{sim} + \alpha L^T L\sigma))$$

**Results:** A phantom (Fig. 1a) was created by placing gelatin slices of increasing thicknesses (5, 10, 15, and 20mm) in a saline-filled container. The conductivity contrast between gelatin and saline was approximately 2:1 (NaCl was added to gelatin resulting in a conductivity of ~1.8 S/m). $CuSO_4$ (an MR contrast agent) was added to the gelatin**,** but not to the saline. An MR amplitude image was acquired on a Philips Achieva 3T platform, with a standard 3D SE sequence (Fig. 1b). Phase data from the 3D SE was recorded and utilized for conductivity image reconstruction. The second spatial derivatives of the phase images were computed with Savitzky-Golay filters using the central point and three adjacent points on each side of the central pixel. Conductivity is reconstructed with Eq. 1 and later smoothed with a Gaussian filter with a standard deviation of two pixels to reduce noise. The resulting image is shown in Fig. 2a; the less conductive gelatin appears darker than the saline. Fig. 2b shows the estimated conductivty distribution reconstructed using the **proposed** inverse formulation. This approach does not exhibit the significant boundary artifacts and lower resolution of Fig. 2a, in which the dependance on derivative computation is sensitive to the image boundary and **stable derivative estimation** requires information from several neighbouring pixels, thus reducing resolution and smoothing sharp changes. Fig. 3 illustrates the fitting process; the green line is the initial guess (uniform conductivity of 0.1 S/m), red is the measured phase, and blue is the fitted phase.

a) Striped gelatin and saline phantom

b) MR signal image and the subdomain used for MR-EPT reconstruction

**Figure 1** - Phantom (a) and its MR magnitude image (b).

a) Laplacian based MR-EPT image reconstruction

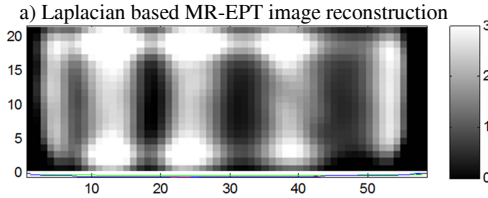


b) New MR-EPT image reconstruction based on the inverse formulation

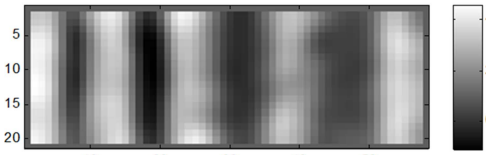


**Figure 2** - MR-EPT Reconstructions: Laplacian based (a) and, inverse formulation based (b).

**Discussion/Conclusion:** The inverse formulation presented here enables conductivity reconstruction by matching the MR-recorded phase information. The primary advantage of this approach is that is does not require differentiation of the phase data. Some smoothing is enforced by a regularization functional, but the strength of this functional can be controlled (e.g. functionals allowing sharp contrast changes, such as Total Variation, can be employed). Another approach, using prior structural information from MRI, can be used to build ad-hoc regularization functionals that permit sharper transitions at particular locations. In summary, we believe the approach proposed and demonstrated here establishes a new technique for reconstructing MR-EPT images which can leverage recent developments in inverse problems and ultimatley produce more clinically useful electrical property images.

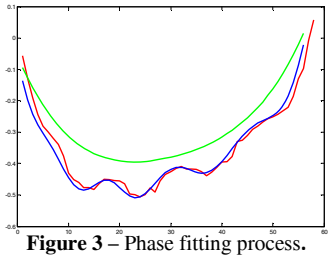

**Figure 3** – Phase fitting process.

# MR-EPT Reconstruction Using an Inverse Formulation


Andrea Borsic[1], Irina Perreard[1,2], Ryan Halter[1]

[1]Thayer School of Engineering, Dartmouth College, Hanover, NH, USA
Radiology Department, Geisel School of Medicine at Dartmouth College, Hanover, NH, USA



## ABSTRACT

We propose a novel approach to imaging electrical properties of tissues with MRI as a variant of the recently developed MR Electrical Properties Tomography (MR-EPT) [1,2]. MR-EPT makes certain simplifications to the Maxwell Equations describing the propagation of the B1 RF field. In particular, the electrical conductivity is shown to be proportional to the Laplacian of the B1 field phase [1]. Computing the Laplacian (second derivatives) of the phase is extremely sensitive to noise and undesirable. A recent approach using Gauss' theorem to expresses conductivity as a surface integral of the gradients of B1 phase, reduces this computation to a first order derivative and makes image reconstruction less sensitive to noise [2]. Here, we propose an inverse formulation, in which the spatial distribution of conductivity is taken as a parameter to be fitted; specifically, a simulated phase is computed from an initial estimate of the conductivity distribution and fitted to the MR measured B1 phase. This has the advantage of not requiring computation of any phase derivatives. This approach is applicable to both MR-EPT conductivity and permittivity imaging, and has the potential of improving MR-EPT in in-vivo applications.


## METHOD

The B1 transmit RF field interacts with a phantom or with a human body and this relationship is generally described by the Helmholtz equation:

$$\nabla^2 \vec{B1} = -\mu\omega^2 k \vec{B1} + \left[\frac{\nabla}{k} \times (\nabla \times \vec{B1})\right] \quad (1)$$

where *B1* is the B1 RF field, $k = \varepsilon - j(\sigma/\omega)$, ε being the electrical permittivity of the medium, σ the electrical conductivity, and ω the angular frequency.
The above relationship for distributions *k* that are slowly varying and isotropic has been simplified and split in two relationships:

$$\sigma \approx \frac{1}{\mu\omega} \nabla^2 \phi(\vec{B1}) \quad (2)$$

$$\epsilon \approx \frac{-1}{\mu\omega^2} \nabla^2 |\vec{B1}| \quad (3)$$

which express electrical conductivity and permittivity as functions of the phase of the B1. In particular σ and ε are shown to be proportional (under the simplifications that lead to these equations) to the Laplacian of respectively the B1 field phase and amplitude. Recovery of these quantities by differentiation is however a process sensitive to noise, particularly as (2) and (3) involve second derivatives. An approach in [2] has been proposed, which uses the Gauss theorem to express σ and ε as surface integrals of the gradient of the phase and amplitude of B1, reducing thus the differentiation order and sensitivity to noise.
In order to completely remove differentiation we propose to adopt an inverse problem formulation. For the reconstruction of conductivity the phase Φ of B1 can be computed from (2) as

$$\nabla^2 \phi = \mu\omega\sigma \quad (4)$$

assuming σ to be known. The phase computed from (4), can be fitted to the measured phase $\Phi_{meas}$ by acting on the distribution σ, leading to an inverse approach for the estimation of σ:

$$\sigma_{rec} = \text{argmin} \|\phi(\sigma) - \phi_{meas}\|^2 + \alpha\Psi(\sigma) \quad (5)$$

where $\sigma_{rec}$ is the reconstructed conductivity, α a scalar value, and ψ a regularization functional. The fitting approach of (5) allows therefore reconstructing the conductivity distribution (or similarly the permittivity distribution) without requiring differentiation of B1 information.
A second advantage of this approach is that the smoothing in the reconstructed image, necessary to mitigate the mild ill-posedness of the problem, is controlled by the regularization functional ψ(σ). It is possible therefore to make different choices for ψ(σ) depending on the type of distribution to be reconstructed or even using ψ(σ) to incorporate prior anatomical information into reconstructions.
In the following we demonstrate the above approach using a traditional quadratic regularization functional and using Total Variation [3], a functional able to reconstruct sharp profiles.

## QUALITATIVE EVALUATION

The proposed approach has been validated experimentally. In a first experiment a phantom was created cutting a gelatin block in slices of progressive thickness (5, 10, 15, 20mm), by inserting the slices in a container (Fig.1A), and by filling the container with a highly conductive saline solution. The gelatin was produced with CuSO4, to create a MR magnitude contrast. Spin Echo magnitude and phase data were collected on a Philips Achieva 3T platform. The magnitude image (Fig.1B) shows the slices as bright regions. From the collected data three different MR-EPT reconstructions where performed. A first reconstruction is based on evaluating the Laplacian in (2) using Savitzky-Golay filters on 5 points, and on smoothing with a Gaussian filter the resulting image for improved noise reduction (Fig.1C). The reconstruction identifies well the gelatin stripes, which show in darker color, as less conductive then the saline solution used to fill the container. Two further reconstructions were performed using the inverse approach. Fig.1D shows a reconstruction using a quadratic regularization terms. This reconstruction is slightly less noisy and more defined compared to the reconstruction in Fig.1C. A second inverse reconstruction uses Total Variation as regularization functional, and is able to produce sharp transitions at the interface between saline and gelatin slices (Fig.1E). Overall these results demonstrate that the inverse approach works well in practice and that different regularization functionals allow choosing different priors in terms of smoothness in the reconstructed image.

Fig 1A - Gelatin Slices and Container

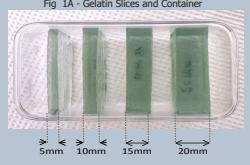


Fig 1B - MR Magnitude

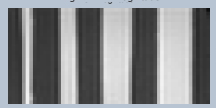

Fig 1C - Average Laplacian Reconstruction

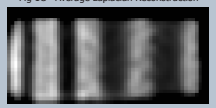

Fig 1D - Inverse Recon Quadratic Regularization

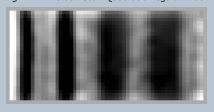

Fig 1E - Inverse Recon TV Regularization

## QUANTITATIVE EVALUATION

For quantitative evaluation purposes a phantom was created by carving circular wells in a block of gelatin. The phantom presents three rows, each with 3 wells with diameters of 5, 10, and 15mm. Fig. 2A shows a magnitude image of the phantom, where the three rows, each with three holes, are visible. The varying well diameter allows evaluating the resolution of MR-EPT as implemented with the prosed algorithm based on an inverse formulation. Each row of the phantom was filled with saline with an increasing conductivity. The row at the bottom has a conductivity of 3 S/m, the middle row of 5 S/m, and the top row of 8 S/m. The block of gelatin has instead an estimated conductivity of 1.8 S/m. MR-EPT reconstructions were performed based on the inverse formulation using a quadratic regularization term and Total Variation regularization, as illustrated respectively in Fig. 2B and 2C. Both reconstruction algorithms identify well the smaller holes of 5mm and provide good quantitative agreement in reconstructed conductivity values, showing an increasing contrast from bottom row to top row, as to be expected. As shown by the colorar, the reconstructed values are close to the original conductivity of the wells.

Fig 2A - MR Magnitude | Fig 2B - Inverse Quadratic Reg | Fig 3C - Inverse TV Reg

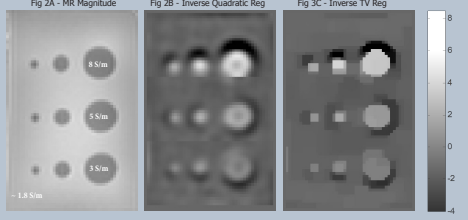


In conclusion reconstruction of MR-EPT conductivity data based on an inverse formulation approach shows potential in terms of not requiring differentiation of the input data, and in terms of allowing choice of regularization functionals. Utilizing regularization functionals such TV results in sharper images. Future work will be conducted in incorporating prior anatomic information through ad-hoc regularization techniques.

### REFERENCES


[1] H. Wen, "Non-invasive quantitative mapping of conductivity and dielectric distributions using the RF wave propagation effects in high field MRI", in Medical Imaging: Physics of Medical Imaging, vol. 5030 of Proceedings of SPIE, pp. 471–477, February 2003.
[2] U. Katscher, T. Voigt, C. Findeklee, P. Vernickel, K. Nehrke, and O. Dossel, "Determination of electrical conductivity and local SAR via B1 mapping", IEEE Transactions on Medical Imaging, vol. 28, pp. 1365–1374, 2009.
[3] Borsic A, Graham BM, Adler A, Lionheart WRB, "In Vivo Impedance Imaging With Total Variation Regularization", IEEE Transactions on Medical Imaging, 29, 1, 44-54, 2010.

# MR-EPT Reconstruction Using an Inverse Formulation

Andrea Borsic[1], Irina Perreard[1, 2], and Ryan J. Halter[1]

[1]Thayer School of Engineering, Dartmouth College, Hanover, NH, USA
[2]Radiology Department, Geisel School of Medicine at Dartmouth College, Hanover, NH, USA

**Abstract:** The electrical conductivity of soft tissues can be reconstructed from imaging with MR Electrical Properties Tomography (MR-EPT). The reconstruction method used here is based on an inverse problem formulation, with two advantages over a direct inversion approach: a) no spatial differentiation is needed and b) the regularization term determines the resolution of the reconstructed data. The process is exemplified using phantom (gelatine and saline) data.

## 1 Introduction

Magnetic Resonance Electrical Property Tomography (MR-EPT) is a relatively new strategy for estimating a tissue's electrical conductivty and permittivity distribution. It offers the potential of high resolution admittance mapping as compared to electrical impedance tomography (EIT) without the need for electrodes as are needed for magnetic resonance EIT (MR-EIT). The general approach for conductivty imaging with MR-EPT is to obtain a phase image and/or B1 map image of the RF field produced using specific pulse sequences. This image can be manipulated to estimate the conductivity distribution. Typically, this manipulation requires second derivatives be computed from the phase data. This is an undesirable process that is prone to amplify noise. Other approaches have included algorithms that lower this requirement to first derivatives, reducing sensitivity to noise. Here we describe an alternative method that solves the MR-EPT problem using an inverse problem formulation that does not require differentiating the input image.

## 2 Methods

### 2.1 Inverse approach formulation

In MR-EPT, the electrical conductivity $\sigma$ can be shown to be proportional to the Laplacian of the phase of the transmit B1 field:

$$\sigma(r) \approx \frac{1}{\omega\mu}\Delta\phi\left(H^{+}(r)\right). \quad (1)$$

The inverse is true as well: if $\sigma(r)$ is known, the phase can be obtained by solving $\Delta\phi = \omega\mu\sigma(r)$. Using an iterative inverse formulation approach, the updated value of σ is given by $\sigma_{new} = \sigma + \delta\sigma$ where

$$\delta\sigma = (J^T J + \alpha L^T L)^{-1}\left(J^T\left(\phi\left(H^{+}(r)\right) - \phi + \alpha L^T L\sigma\right)\right). \quad (2)$$

Here $J$ is the Jacobian of the conductivity to phase mapping, $L$ is a regularization matrix, and $\alpha$ is a regularization parameter used to stabilize the inversion. We have implemented this inversion using two different regularization terms: a) a quadratic/Laplacian approach and b) a Total Variation functional approach [1,2]. A Primal Dual Interior Point Method optimization scheme is used for the Total Variation approach, which produces images with sharper contrasts at boundaries.

### 2.2 Data acquisition

A custom gelatin phantom (10% gelatin, 1% NaCl) was constructed with three rows of circular wells with increasing diameters (5, 10, 15mm). Each series of wells was filled with saline solutions with increasing conductivities (~3, 5, 8 S/m). Cupric sulphate was added for MR contrast (Figure 1). Data was acquired on a Philips Achieva 3T platform, with a standard 3D SE sequence; phase images were used for reconstructing the conductivity. Two-dimensional reconstructions of the electric conductivity based on our inverse approach are presented in Figure 2.

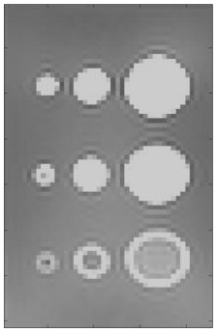

**Figure 1:** Phantom geometry (MR magnitude).

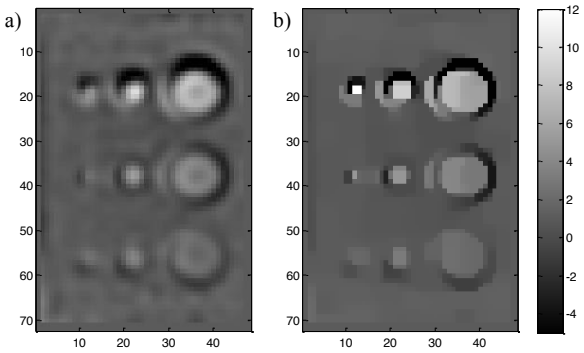


**Figure 2:** MR-EPT reconstruction with the inverse formulation approach: a) with quadratic regularization; b) with Total Variation regularization.

## Conclusions

Reconstruction of MR-EPT conductivity data based on an inverse formulation approach is demonstrated here. The primary advantage of this approach is that is does not require differentiation of the phase data. An additional advantage is that custom regularization approaches can be considered for enahncing image quality. For instance, a priori anatomical information obtained from other MR variants (i.e. T2-weigted imaging) might be used as spatial priors.

## References

[1] Borsic A, Graham BM, Adler A, Lionheart WRB, *IEEE Transactions on Medical Imaging*, 29, 1, 44-54, 2010.
[2] Borsic A, Adler A, *Inverse Problems*, 28, 095011, 2012.

# MR-EPT Reconstruction Using an Inverse Formulation

Andrea Borsic
Irina Perreard
Ryan Halter

# MR-EPT Background

MR-EPT = technique for estimating electrical properties - conductivity and permittivity - of tissues based on MRI technology [1,2] utilizing the phase and magnitude of the B1 field

$$\nabla^2 \vec{B1} = -\mu\omega^2 k \vec{B1} + \left[\frac{\nabla}{k} \times (\nabla \times \vec{B1})\right]$$

$$\sigma \approx \frac{1}{\mu\omega}\nabla^2\phi(\vec{B1}) \qquad\qquad \epsilon \approx \frac{-1}{\mu\omega^2}\nabla^2|\vec{B1}|$$

- no electrodes needed

[1] U. Katscher et al., IEEE Trans. on Medical Imaging, vol. 28, pp. 1365–1374, 2009

[2] U. Katscher, Dong-Hyun Kim, and Jin Keun Seo, Comp.and Math. Meth. in Medicine, vol. 2013, Article ID 546562, 2013

# MR-EPT Inverse Approach

The electrical conductivity:

$$\nabla^2 \phi = \mu \omega \sigma$$

$$\phi(r) = \phi(r)_{meas} \quad \forall r \in \partial\Omega$$

The iterative process:

$$\sigma_{rec} = \text{argmin} \| \phi(\sigma) - \phi_{meas} \|^2 + \alpha \Psi(\sigma)$$

Two different regularization terms:

a) a quadratic/Laplacian approach
b) a Total Variation functional approach[1,2] using a Primal Dual Interior Point Method optimization scheme

[1]Borsic A, Graham BM, Adler A, Lionheart WRB, *IEEE Transactions on Medical Imaging*, 29, 1, 44-54, 2010.
[2]Borsic A, Adler A, *Inverse Problems*, 28, 095011, 2012.

# Numerical simulations

"Test Conductivity Cube" 20x20x20 pixels

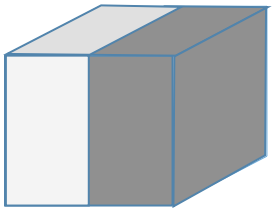

σ1 = 2 S/m  σ1 = 1 S/m

Finite Difference Solver

Slice 10 in the xz plane

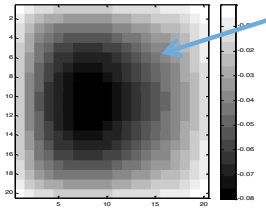

More conductive region
-> stronger Laplacian

Cross Section Plot

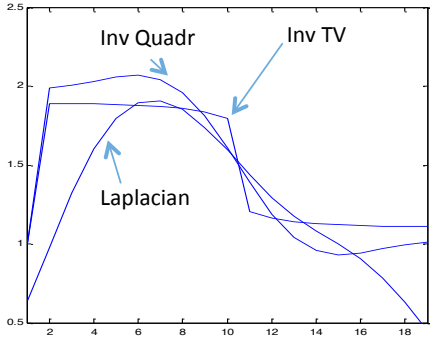


Full 3D Recons, data presented in the same slice as above

3D Laplacian with 5 point derivative estimation

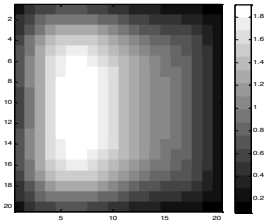

3D Inverse Quadratic Regularization Tik = 3e-5

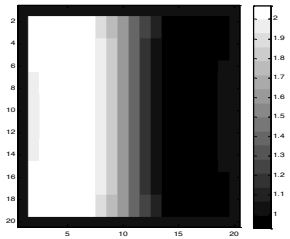

3D Inverse TV Regularization Tik = 3e-5

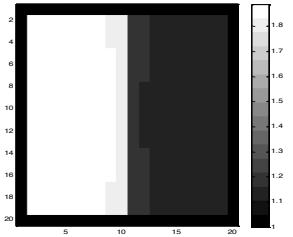

# Data acquisition – gelatin* phantoms

**Multiple homogeneous inclusions**

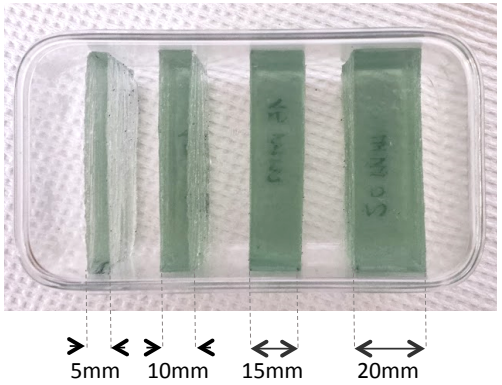


~1.8 S/m gelatin slices
4.1 S/m saline
MR contrast!

**Multiple inclusions heterogeneous**

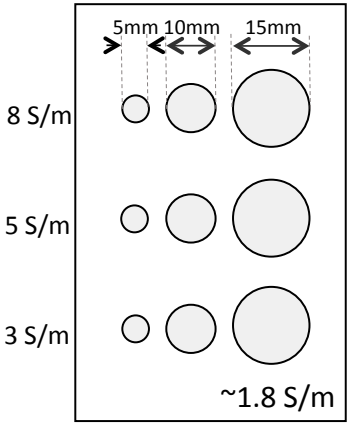


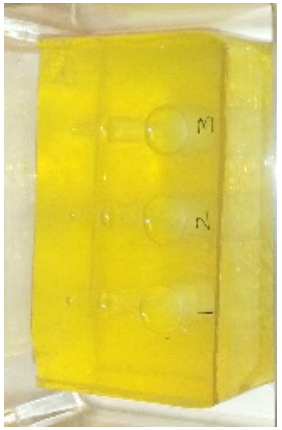

assessing spatial resolution

**Gelatin prostate**

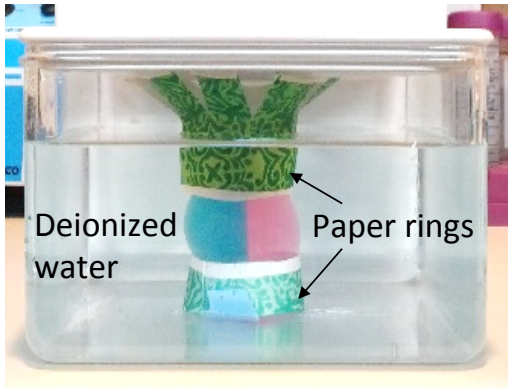


CT of a real prostate
Pink 1.6 S/m / blue 3.4 S/m

**Imaging:** Philips Achieva 3T +2 channel flex coil, MS Spin Echo sequence: TR=800, TE=20, NSA=16, 2x2x3 mm voxel

*Gelatin = Sterile water + % NaCl + 10% Gelatin

# Reconstructions

**Multiple homogeneous inclusions phantom**

SE magnitude

3D avg laplacian

3D inverse recon

2D TV inverse recon

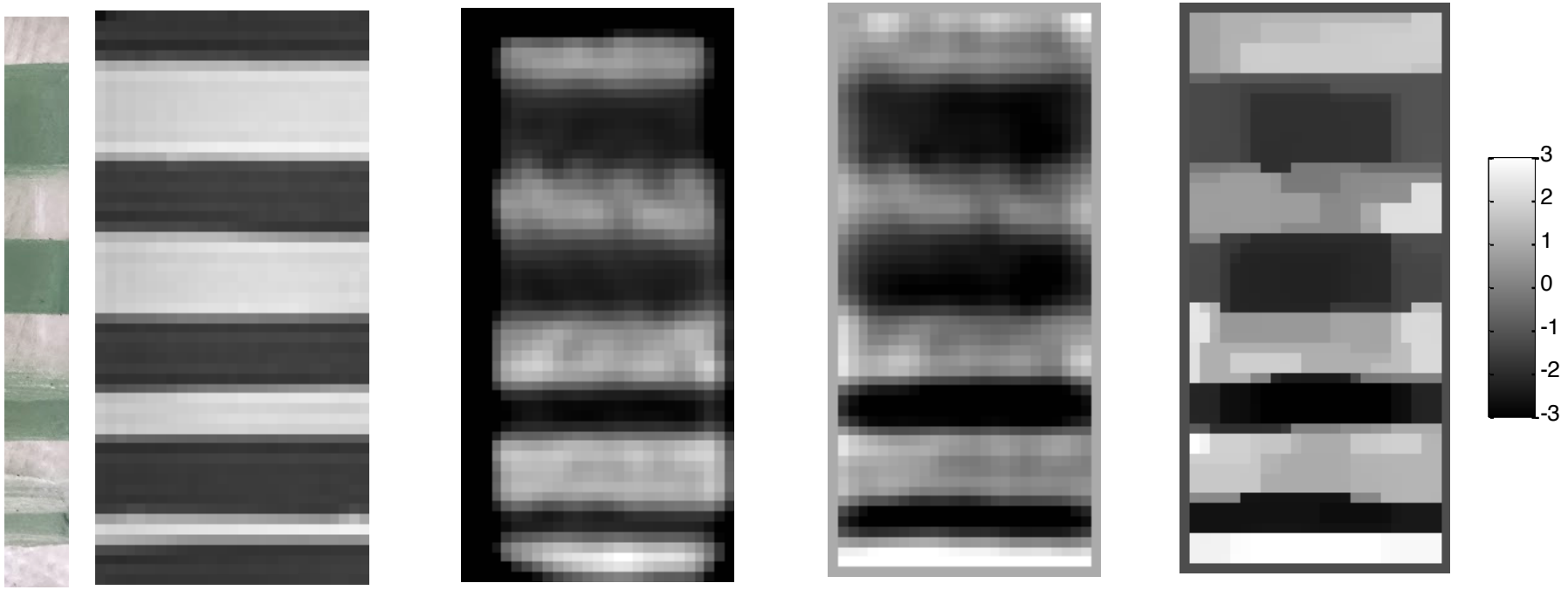

# Reconstructions

**Multiple inclusions heterogeneous phantom**

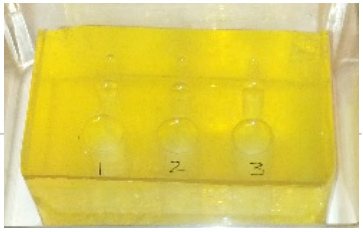


SE magnitude

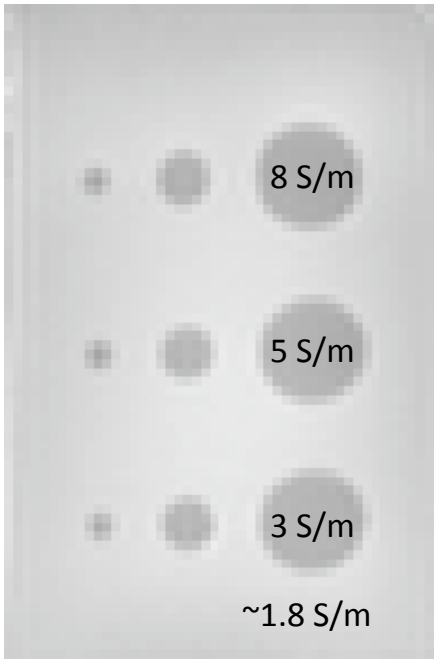


3D avg laplacian

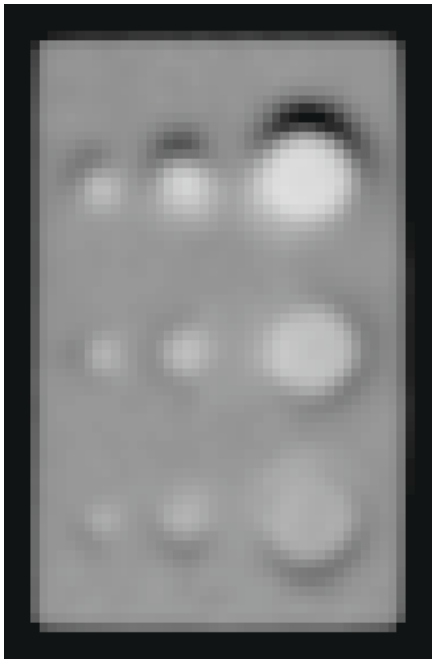

3D inverse recon

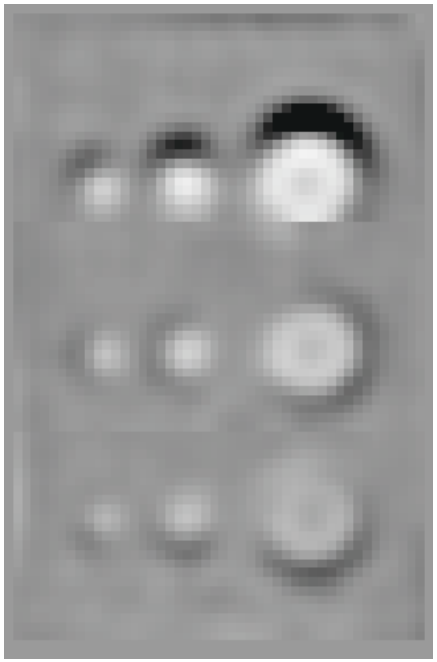

TV 2D inverse recon

# Reconstructions

**Gelatin prostate phantom**

SE magnitude

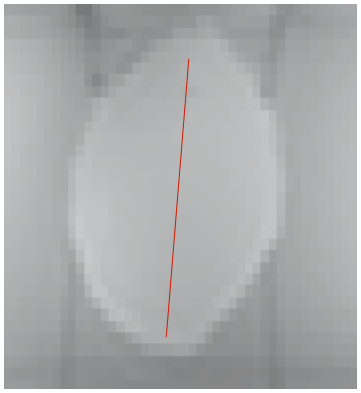

3D avg laplacian

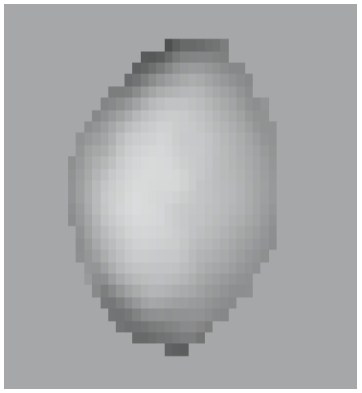

3D inverse recon

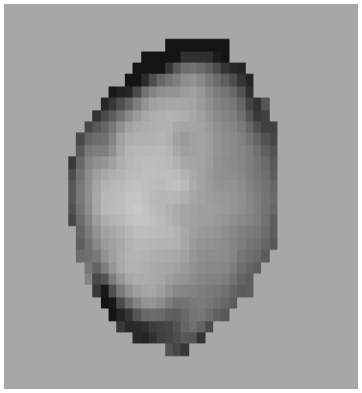

2D TV inverse recon

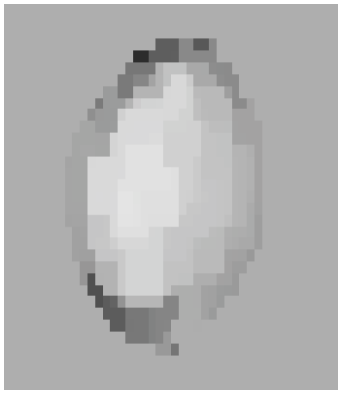

# Conclusion

Successful reconstruction electrical conductivity using an inverse approach

- Spatial accuracy
- Qualitative match

Under progress: MR-EPT reconstructions of permittivity

Future clinical applications: currently implementing the imaging protocol for an ex-vivo prostate study

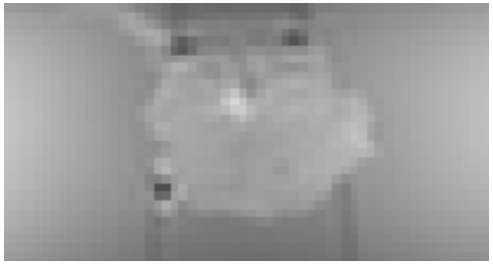

SE magnitude

3D conductivity reconstruction

# Acknowledgements

Prof. John Weaver

***Advanced Imaging Center at DHMC:***

Michael Pearl

John Peiffer

***Funding:***

DOD W81XWH-13-1-0127

Dr. Seuss properties ™

Thank you!

Questions?